

EXPERIMENTAL ANALYSIS AND FEA MODELING OF
SENSOR RESPONSE IN COMPOSITES FOR
STRUCTURAL HEALTH MONITORING

by

AKSHATA NAGABHUSHANA

SUSAN BURKETT, COMMITTEE CHAIR

SAMIT ROY
MARK BARKEY

A THESIS

Submitted in partial fulfillment of the requirements
for the degree of Master of Science
in the Department of Electrical and Computer Engineering
in the Graduate School of
The University of Alabama

TUSCALOOSA, ALABAMA

2012

Copyright Akshata Nagabhushana 2012
ALL RIGHTS RESERVED

ABSTRACT

Reliable damage detection is crucial for assessing the integrity of a structure. A structural health monitoring (SHM) system reduces the chances of fatal accidents by performing continuous monitoring of a structure. In this thesis, a well-established SHM technique, the Lamb wave-based approach, is used for damage detection in composite materials. Composite coupons are fabricated using a vacuum assisted resin transfer molding (VARTM) process. The damage to be detected is a pre-existing transverse crack in the coupon. Surface mounted piezoelectric actuators are used to generate Lamb waves in the composite coupon. Experiments were carried out on a composite coupon with a manufactured embedded crack-like defect in the middle four plies for two different orientations, $[0_{16}]_T$ and $[0_6/90_4/0_6]_T$, and a composite coupon with a surface crack with $[0_{16}]_T$ orientation. The response from both undamaged and damaged (simulated crack) coupons is obtained using surface mounted piezoelectric sensors. A numerical study of the composite coupon with the simulated crack was conducted using finite element methods (FEM) and the model was verified using the experimental results. The FEM model is validated for crack modeling using static shear lag analysis applied at the crack as well as for dynamic loading. The active Lamb wave method, using the anti-symmetric mode, could detect a surface crack but was insensitive to the embedded crack. The effect of crack depth and crack location on damage detection efficiency was also studied. FEM models were also used for sensor placement optimization.

LIST OF ABBREVIATIONS

| | | |
|---------|---|---|
| AFC | – | Active fiber composite |
| ANN | – | Artificial neural network |
| CFRP | – | Carbon fiber reinforced polymer |
| CLT | – | Classical lamination theory |
| DAQ | – | Data acquisition |
| FBG | – | Fiber bragg grating |
| FEM | – | Finite element method |
| FOS | – | Fiber optic sensors |
| GPIB | – | General purpose interface bus |
| MFC | – | Macro fiber composite |
| NDE | – | Non-destructive evaluation |
| PT | – | Lead titanate |
| PVDF | – | Polyvinylidene fluoride |
| PZT | – | Lead zirconate titanate |
| RTM | – | Resin transfer molding |
| SHM | – | Structural health monitoring |
| SNOBFIT | – | Stable nosiy optimization by branch and fit |
| SPO | – | Sensor placement optimization |
| SVM | – | Support vector machine |
| VARTM | – | Vacuum assisted resin transfer molding |

ACKNOWLEDGEMENTS

I'm extremely grateful to my advisor Dr. Susan Burkett, for the technical guidance, encouragement, and academic advice. Dr. Burkett has been a great support and true inspiration to me throughout the course of my graduate studies. I'm thankful to her for having faith in me and motivating me to excel all the time. I would like to express my sincere gratitude to my thesis committee members, Dr. Samit Roy and Dr. Mark Barkey for their time, valuable advice and feedback. Their vast knowledgebase was extremely helpful. They made every technical discussion I had with them fruitful, inspiring and productive. I'm indebted to their technical support and encouragement.

I'm thankful to Dr. Sushma Kotru for giving valuable inputs and encouraging me to perform as one of her own student. Special thanks to her for letting me use few of the equipment from her lab. I sincerely appreciate Dr. Edward Sazonov's time and suggestions. This work would not have been possible without the support and assistance of my entire SHM group, Donald Tyler Paul, Nicholas Hayes, Stephen Adu, Ben Fairbee, Kanchan Trivedi, Michelle Spiegel, Hao Zheng, and Muhammad Farooq. Millions thanks to the group for helping in composite fabrication, experimental and numerical testing, and optimization. Thanks to the optimization team for letting me use one of their result. Special thanks to Michelle Spiegel and Kanchan Trivedi, fellow graduate students and friends for being there for me all the time. Their cheerful nature and sense of humor made the entire project work all the more enjoyable.

This work was supported by the United States National Aeronautics and Space Administration, grant number: NNX10AJ14G; Technical monitor, Dr. Curtis E. Banks, NASA MSFC. I gratefully acknowledge the financial and technical support.

I'm indebted to University of Alabama, Tuscaloosa for embracing me whole heartedly and giving me the kind of knowledge and exposure I had only dreamt of.

I'm greatly thankful to my husband Madhav Rao, my best friend and soul mate. He has been my source of strength and has always led by example. If not for him, this graduate program would not have been possible. Finally I would like to thank my parents and in-laws for their unconditional support and encouragement.

CONTENTS

| | |
|---|-----|
| ABSTRACT | ii |
| LIST OF ABBREVIATIONS | iii |
| ACKNOWLEDGEMENTS | iv |
| LIST OF TABLES | ix |
| LIST OF FIGURES | x |
| CHAPTER 1. INTRODUCTION | 1 |
| CHAPTER 2. BACKGROUND | 6 |
| 2.1 Introduction to Lamb waves..... | 6 |
| 2.2 Lamb wave methods..... | 7 |
| 2.3 Sensing methods..... | 8 |
| 2.4 Piezoelectric transducers and principle of operation..... | 9 |
| 2.5 Actuation parameters..... | 10 |
| 2.6 Transverse crack..... | 12 |
| 2.7 Finite element analysis | 12 |
| 2.8 Finite element analysis for optimization | 13 |
| CHAPTER 3. FABRICATION OF COMPOSITE PANEL..... | 15 |
| CHAPTER 4. EXPERIMENTAL ANALYSIS..... | 18 |

| | | |
|--|---|----|
| 4.1 | Data acquisition setup | 18 |
| 4.2 | Test for damage detection | 20 |
| 4.2.1 | Simulated damage using drilled holes in a laminate..... | 20 |
| 4.2.2 | Simulated damage using a fabricated transverse surface crack | 22 |
| 4.2.3 | Simulated damage using a fabricated transverse embedded crack | 23 |
| CHAPTER 5. FINITE ELEMENT ANALYSIS | | 25 |
| 5.1 | Composite benchmark test | 25 |
| 5.2 | Dynamic simulation benchmark tests | 32 |
| 5.3 | Crack modeling benchmark tests | 35 |
| 5.4 | PZT modeling..... | 38 |
| 5.5 | Transverse crack detection using Lamb wave..... | 39 |
| 5.5.1 | Embedded crack model..... | 39 |
| 5.5.2 | Surface crack modeling..... | 41 |
| 5.5.3 | Embedded crack at various depth | 44 |
| 5.5.4 | A surface crack at various locations | 45 |
| CHAPTER 6. RESULTS AND DISCUSSION..... | | 48 |
| 6.1 | Comparison of experimental and modeling results..... | 48 |
| 6.2 | FFT analysis | 50 |
| 6.2.1 | FFT analysis of an embedded crack..... | 50 |
| 6.2.2 | FFT analysis of a surface crack | 53 |
| 6.2.3 | FFT analysis of a crack at various depths | 55 |

| | | |
|--|--|----|
| 6.2.4 | FFT analysis of a surface crack at various locations | 57 |
| CHAPTER 7. FINITE ELEMENT MODEL FOR OPTIMIZATION | | 61 |
| 7.1 | Interface between MATLAB and Abaqus | 61 |
| 7.2 | Embedded crack test..... | 63 |
| CHAPTER 8. CONCLUSIONS AND FUTURE WORK..... | | 65 |
| 8.1 | Conclusions | 65 |
| 8.2 | Recommendations for future work..... | 66 |
| REFERENCES | | 68 |
| APPENDIX A: Conference contributions | | 74 |
| APPENDIX B: LabVIEW program..... | | 75 |

LIST OF TABLES

| | |
|---|----|
| Table 5.1. Material properties of IM7/PETI5 composite used for benchmarking tests [60]. | 26 |
| Table 5.2. Material properties of IM7/PETI5 composite used for benchmarking tests (re-written using SI units). | 26 |
| Table 5.3. Comparison of the exact solution and the Abaqus solution for von Mises longitudinal, transverse and shear stresses for different types of elements. | 28 |
| Table 5.4. Comparison of the exact solution and the Abaqus solution for deflection observed in a specially orthotropic symmetric composite plate for different types of elements. | 31 |
| Table 5.5. Comparison of the exact solution and the Abaqus solution for deflection observed in an off-axis symmetric composite plate for different types of elements. | 31 |
| Table 5.6. Material properties of aluminum for the dynamic simulation test. | 32 |
| Table 5.7. Material properties of the IM7/SC780 composite coupon. | 36 |
| Table 6.1. A table of RMS deviation between a $[0_{16}]_T$ undamaged coupon and coupons with a surface crack of various depths. | 54 |
| Table 6.2. A table of RMS deviation between a $[0_{16}]_T$ undamaged composite coupon and coupons with a four ply deep crack at various depths along the coupon. | 57 |
| Table 6.3. A table of RMS deviation between a $[0_{16}]_T$ undamaged composite coupon and coupons with a four ply deep surface crack at various locations across the coupon. | 59 |

LIST OF FIGURES

| | |
|---|----|
| Figure 1.1. A pictorial representation of material composition of the Boeing 787 dreamliner [2]..... | 1 |
| Figure 1.2. Photographs of structural failures leading to accidents due to corrosion and fatigue: a) the Aloha Airlines flight showing the ruptured aircraft skin [6] and b) I-35W Minnesota bridge collapse [7]..... | 2 |
| Figure 2.1. Graphical representation of Lamb wave modes: a) anti-symmetric and b) symmetric..... | 7 |
| Figure 2.2. A typical PZT excitation input signal for the testing scheme used in this study..... | 11 |
| Figure 3.1. Two photographs to illustrate composite panel fabrication stages: a) fabric layup and b) resin infusion..... | 16 |
| Figure 3.2. Two photographs to illustrate composite panel fabrication stages: a) the final cured composite panel and b) coupons trimmed from the composite panel. | 17 |
| Figure 4.1. Data acquisition system using PZT actuators and sensors. | 19 |
| Figure 4.2. A pictorial representation of a damaged composite coupon illustrating the actuator and sensor placement. | 20 |
| Figure 4.3. Experimental test results comparing the Lamb wave response of an undamaged coupon and coupons with varying hole size..... | 21 |
| Figure 4.4. A pictorial representation of a composite coupon with four 3.175 mm diameter holes illustrating the actuator and sensor placement relative to the holes. | 21 |
| Figure 4.5. Experimental test results comparing the Lamb wave response of an undamaged coupon and coupons with varying number of holes. | 22 |
| Figure 4.6. A pictorial representation of a composite coupon with a surface crack demonstrating the actuator and sensor placement relative to the crack..... | 23 |
| Figure 4.7. Experimental results comparing the Lamb wave response of a $[0_{16}]_T$ orientation undamaged coupon and a coupon with a surface crack in the first four plies. | 23 |
| Figure 4.8. A pictorial representation of a composite coupon with an embedded crack demonstrating the actuator and sensor placement relative to the crack..... | 24 |

| | |
|---|----|
| Figure 4.9. Experimental results comparing the Lamb wave response of an undamaged coupon and a coupon with an embedded crack for: a) a $[0_{16}]_T$ composite coupon and b) a $[0_6/90_4/0_6]_T$ composite coupon. | 24 |
| Figure 5.1. FE model of a composite coupon representing the load and boundary conditions for a pull test. | 26 |
| Figure 5.2. Abaqus results showing the von Mises stress contour legends of the longitudinal and transverse stresses (in Pa) for a composite coupon modeled with S4R elements under an axial displacement load. | 27 |
| Figure 5.3. FE model of a composite plate meshed with 2D shell elements representing the load and boundary conditions. | 29 |
| Figure 5.4. Abaqus results showing the deflection contour plot for a 2D shell composite plate under uniform transverse pressure load. | 29 |
| Figure 5.5. FE model of a composite plate meshed with 3D brick elements representing the load and boundary conditions. | 30 |
| Figure 5.6. Abaqus results showing the deflection contour plot for a 3D brick composite plate under uniform transverse pressure load. | 30 |
| Figure 5.7. 3D FE model of an aluminum beam representing load and boundary conditions for the dynamic simulation test. | 32 |
| Figure 5.8. Abaqus results showing the deflection contour plot and legend for the dynamic simulation test in m. | 33 |
| Figure 5.9. Comparison of exact deflection solution and Abaqus solution for an aluminum beam meshed with 2 elements and subjected to a dynamic load. | 34 |
| Figure 5.10. Comparison of exact deflection solution and Abaqus solution for an aluminum beam meshed with 4 elements and subjected to a dynamic load. | 34 |
| Figure 5.11. Comparison of exact deflection solution and Abaqus solution for an aluminum beam meshed with 8 elements and subjected to a dynamic load. | 35 |
| Figure 5.12. a) Abaqus stress contour plot for a composite coupon with two cracks under an axial load and b) an enlarged and exaggerated view near the crack showing the crack opening. | 37 |
| Figure 5.13. Comparison of shear lag model and Abaqus model results for a composite coupon with two transverse cracks. | 37 |
| Figure 5.14. Material properties of piezoelectric actuators/sensors used in this study. | 38 |
| Figure 5.15. Pictorial representations of $[0_{16}]_T$ and $[0_6/90_4/0_6]_T$ composite coupons with an embedded crack in the middle four plies. | 39 |

| | |
|---|----|
| Figure 5.16. Abaqus models showing the embedded crack in a $[0_{16}]_T$ composite coupon: a) a wireframe model representation and b) a mesh representation..... | 40 |
| Figure 5.17. Finite element (FE) results comparing the lamb wave response of an undamaged coupon and a coupon with an embedded crack for: a) a $[0_{16}]_T$ composite coupon and b) a $[0_6/90_4/0_6]_T$ composite coupon. | 41 |
| Figure 5.18. Finite element (FE) results comparing the lamb wave response of an undamaged coupon and a coupon with an embedded crack for: a) a $[0_{16}]_T$ composite coupon and b) a $[0_6/90_4/0_6]_T$ composite coupon for larger actuator. | 41 |
| Figure 5.19. Pictorial representation of a $[0_{16}]_T$ composite coupon with surface cracks of varying depth: a) a surface crack in the first 4 plies; b) a surface crack in the first 3 plies; c) a surface crack in the first 2 plies; and d) a surface crack in the first ply only. | 42 |
| Figure 5.20. Finite element results comparing the lamb wave response of an undamaged $[0_{16}]_T$ composite coupon and a coupon with a surface crack for: a) a surface crack in the first 4 plies; b) a surface crack in the first 3 plies; c) a surface crack in the first 2 plies; and d) a surface crack in the first ply only. | 43 |
| Figure 5.21. Pictorial representation of a $[0_{16}]_T$ composite coupon with a 4 ply deep embedded crack in: a) 2 nd to 5 th ply; b) 3 rd to 6 th ply; and c) 7 th to 10 th ply. | 44 |
| Figure 5.22. Finite element results comparing the Lamb wave response of a $[0_{16}]_T$ undamaged coupon and a coupon with a 4 ply deep embedded crack in: a) 2 nd to 5 th ply and b) 3 rd to 6 th ply. | 45 |
| Figure 5.23. Pictorial representation of a $[0_{16}]_T$ composite coupon with a surface crack in the first four plies located: a) near the actuator end; b) in the middle; and c) near the sensor end. | 46 |
| Figure 5.24. Finite element results comparing the Lamb wave response of a $[0_{16}]_T$ oriented undamaged coupon and a coupon with a surface crack in the first four plies located: a) near the actuator end; b) in the middle; and c) near the sensor end. | 47 |
| Figure 6.1. Comparison of experimental and Abaqus modeling results for an undamaged coupon. | 49 |
| Figure 6.2. Comparison of experimental and Abaqus modeling results for an undamaged coupon after adjusting the modulus. | 49 |
| Figure 6.3. FFT spectrum based on Abaqus results comparing the frequency response of a $[0_{16}]_T$ orientation undamaged coupon and a coupon with an embedded crack in the middle four plies. | 51 |
| Figure 6.4. Enlarged view of a FFT spectrum at frequencies near 976.6 Hz showing less than 1% difference between the frequency response of a $[0_{16}]_T$ orientation undamaged coupon and a coupon with an embedded crack in the middle four plies. | 51 |

| | |
|--|----|
| Figure 6.5. FFT spectrum based on Abaqus results comparing the frequency response of a $[0_6/90_4/0_6]_T$ orientation undamaged coupon and a coupon with an embedded crack in the middle four plies. | 52 |
| Figure 6.6. Enlarged view of a FFT spectrum at frequencies near 976.6 Hz showing less than 2% difference between the frequency response of a $[0_6/90_4/0_6]_T$ orientation undamaged coupon and a coupon with an embedded crack in the middle four plies..... | 52 |
| Figure 6.7. Complete FFT spectrum for $[0_{16}]_T$ composite coupons comparing the frequency response of undamaged to damaged coupons that is provided by varying the depth of a surface crack. | 53 |
| Figure 6.8. An enlarged view of FFT spectrum for an $[0_{16}]_T$ undamaged composite coupon and coupons with a surface crack of various depths for frequencies near: a) 976.6 Hz and b) 7.617 kHz. | 54 |
| Figure 6.9. A graphical representation of RMS deviation between a $[0_{16}]_T$ undamaged coupon and coupons with a surface crack of various depths as a function of crack depth..... | 55 |
| Figure 6.10. Complete FFT spectrum for $[0_{16}]_T$ composite coupons comparing the frequency response of an undamaged coupon to coupons with a four ply deep crack at various depths. | 56 |
| Figure 6.11. An enlarged view of a FFT spectrum for an $[0_{16}]_T$ undamaged composite coupon and coupons with a four ply deep surface crack at various depths at frequencies near: a) 976.6 Hz and b) 7.617 kHz. | 56 |
| Figure 6.12. A graphical representation of RMS deviation between a $[0_{16}]_T$ undamaged composite coupon and coupons with a four ply deep crack at various depths as a function of crack location. | 57 |
| Figure 6.13. Complete FFT spectrum for $[0_{16}]_T$ composite coupons comparing the frequency response of undamaged coupon to coupons with a four ply deep surface crack at various locations across the coupon. | 58 |
| Figure 6.14. Enlarged view of FFT spectrum for an $[0_{16}]_T$ undamaged composite coupon and coupons with a four ply deep surface crack at various locations at frequencies near: a) 976.6 Hz and b) 7.617 kHz..... | 59 |
| Figure 6.15. A graphical representation of RMS deviation between an $[0_{16}]_T$ undamaged composite coupon and coupons with a four ply deep surface crack at various locations across the coupon..... | 60 |
| Figure 7.1. A flow chart demonstrating the interface between MATLAB and Abaqus that used for generating data set for sensor placement optimization (where count is the iteration number)..... | 62 |
| Figure 7.2. A FE representation of longitudinal strain component contour plot observed on the top surface of a composite coupon with an embedded crack in the middle..... | 63 |

Figure 7.3. A flow chart demonstrating the sensor placement optimization process.63

Figure 7.4. Random placement of sensors at the beginning of optimization algorithm
(dots represent sensors).....64

Figure 7.5. Final placement of sensors after the completion of optimization algorithm
(dots represent sensors).....64

CHAPTER 1

INTRODUCTION

Carbon fiber reinforced polymer (CFRP) composite materials have gained widespread use over the past two decades in the aerospace and automobile industries and are used extensively in aircraft, space craft, pressure vehicles, fuel tanks, satellites, supercars, racing bicycles, etc. The Boeing 787 dreamliner contains 80% composites by volume that accounts for 50% of the total weight [1]. The material composition of the Boeing 787 is shown in Figure 1.1 [2]. The strong inclination towards CFRP is due to the material's high specific stiffness and strength ratio, good corrosion resistance, and light weight. In addition, it can be tailored to increase the strength in a particular direction or adjust the thermal expansion co-efficient of the material for a specific application.

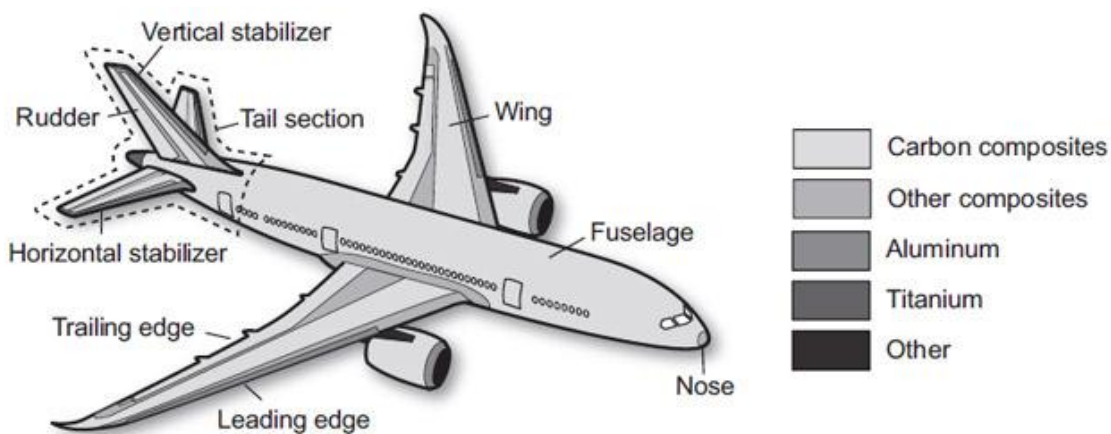


Figure 1.1. A pictorial representation of material composition of the Boeing 787 dreamliner [2].

Composite materials, nonetheless, are susceptible to damage because of fatigue loading, impact, and environmental effects. The analysis of damage in composite materials with variable orientation layup and ply numbers is complicated compared to metals. Failure modes include fiber breakage, fiber matrix debonding, matrix cracking, and delamination [3].

To ensure performance and to improve the lifespan of composite structures, damage detection early in the life cycle is important. There has been a significant amount of research in the area of damage detection in composite materials using an array of strategically placed actuator-sensor combinations.

Several tragic accidents have occurred that motivate this field of research. The structural failure on Aloha Airlines flight 243 [4], the collapse of the I-35W bridge in Minneapolis, the fatigue failure of the Point Pleasant bridge spanning the Ohio river, a structural deficiency in the Seongsu bridge, and the Columbia space shuttle tragedy [5], emphasize the need for periodic structural inspection. Photographs illustrating two of these accidents are shown in Figure 1.2.

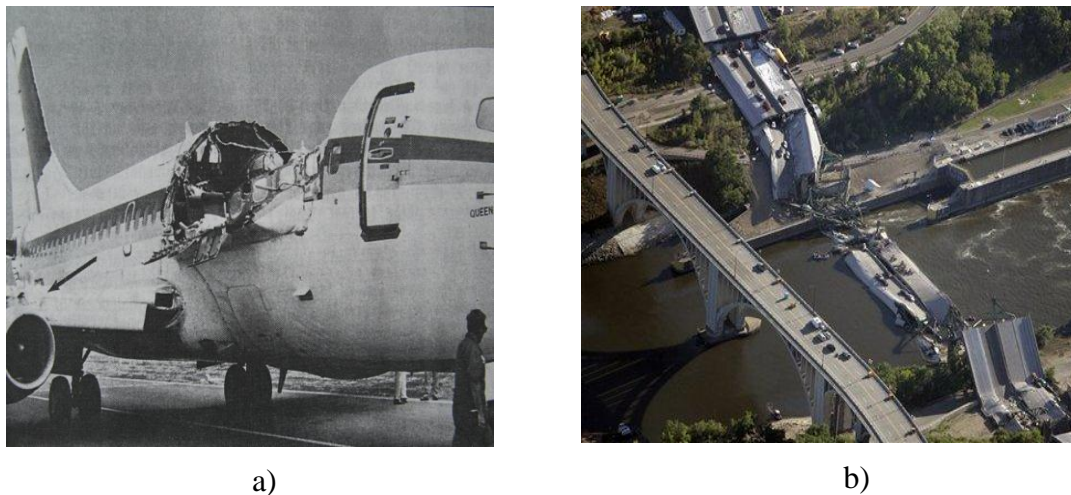


Figure 1.2. Photographs of structural failures leading to accidents due to corrosion and fatigue: a) the Aloha Airlines flight showing the ruptured aircraft skin [6] and b) I-35W Minnesota bridge collapse [7].

Structural health monitoring (SHM) is a field of study involving damage detection techniques intended to avoid catastrophic failure of structures. This practice has become mandatory for some important applications in civil and aerospace engineering. Metis Design Corporation has partnered with the U.S. Navy, Air Force, and NASA to provide SHM solutions to rotorcraft, aircraft and unmanned aerial vehicles [8]. The Boeing 787 has an aircraft health monitoring plan in place to provide real-time data to self-monitor [9].

Structural health monitoring helps in predicting the remaining useful life of a structure by detecting the existence of damage, determining the nature and severity of the damage, and localizing the damage. SHM offers enormous improvements in safety records in addition to the economic benefit. By shifting to a condition-based maintenance approach from the traditional time-based maintenance approach, SHM saves money, unnecessary maintenance downtime, and reduces the chances of catastrophic failures.

SHM evolved from non-destructive evaluation (NDE) techniques in which sensors and actuators are external to a structure and the sensing probes can be adjusted and manipulated to extract the maximum signal. The damage detection methods used in NDE are completely non-obtrusive and safe. The testing occurs only at scheduled intervals. A few examples of NDE include: visual inspection, infrared thermography [10], laser ultrasound [11], laser shearography [12], and X-ray radiography [13]. However, in SHM, the locations of sensors and actuators are fixed and remain on the structure continuously, so are not completely non-obtrusive. This integrated sensing scheme allows for continuous monitoring and provides important information on the evolution of damage. In addition, SHM involves less human intervention compared to NDE techniques and the structure does not have to be taken out of service during structural health testing.

A typical SHM process involves implementation evaluation, data acquisition and damage feature extraction, and classification. Implementation evaluation includes studying the economic and human life safety advantages, possible damage types, operational and environmental conditions, cost and maintenance needs, and the time requirement for deploying the SHM system. The data acquisition portion of the process involves a decision about the number and type of sensors, placement of sensors, type of actuation, acquisition hardware, signal transmission hardware and data storage. A signal processing step is typically performed after data acquisition to cleanse and remove any noise from the data. In feature

extraction, damage sensitive features such as the natural frequency of vibration, strain, time of flight, displacement, and modal shape, are separated out while also compensating for any environmental effects. As a final step, a statistical analysis of acquired data leads to a classification of the structure as damaged or undamaged [14].

Damage detection can be done using either active or passive approaches. In an active approach, actuators such as a piezoelectric patch or a macro fiber composite (MFC) are used to cause perturbations in a structure whereas in a passive approach, a disturbance caused by damage, ambient vibrations, or impact is the source of actuation [15]. Active SHM provides improved control of excitation parameters. In both approaches, surface mounted or embedded sensors are used to receive the response from a structure. Kessler *et al.* [16] proposed the use of a combination of passive and active sensing for SHM. The proposed idea was to perform global damage detection in real time using a passive approach with local damage detection done using an active approach to characterize the damage location, severity, and type. This concept was shown to be effective by Mal *et al.* [17]. Passive SHM can be performed by acoustic emission testing using tomography or impact measurements using foil gauges or piezoelectric sensors [17, 18] and two examples of active SHM approaches are the electrical impedance method and the Lamb wave technique.

Damage detection using Lamb waves and electrical impedance methods are both well-established techniques. In this thesis, a Lamb wave-based approach for detecting damage in composite materials is described. One type of damage commonly observed in composite structures, a transverse crack, was considered for damage detection experiments. A surface mounted piezoelectric actuator was used to generate Lamb waves in a composite structure and the response was measured using a surface mounted piezoelectric sensor. The experimental findings were used to validate the models developed using finite element methods (FEM). Finite element analysis is a critical part of design validation and is useful in

predicting an optimum testing scheme for large and complex structures [19]. This aspect of the research involves optimization of testing parameters, sensor location and the number of sensors.

The thesis is divided into eight chapters. Chapter 2 provides a brief background of the Lamb wave technique, a description of the different sensors used in SHM applications and a summary of related modeling simulations performed by other researchers. In this chapter an overview is also presented of previous research related to this field. The procedure for fabricating undamaged and damaged composite panels is presented in Chapter 3. Details for the detection system used to detect an embedded crack and a surface transverse crack in a composite coupon, along with corresponding experimental results, are reported in Chapter 4. Chapter 5 describes the finite element models used in this project to understand Lamb wave interactions with a crack. Finite element models, using the commercially available finite element code Abaqus, were used and include benchmark tests for crack modeling and dynamic simulation and the Lamb wave models for embedded and surface transverse cracks. The frequency domain information along with finite element analysis was used to characterize the damage. The fast Fourier transform (FFT) results and conclusions of the study are summarized in Chapter 6. Chapter 7 provides a brief description of interfacing MATLAB, Abaqus and optimization algorithms that can be used for sensor placement optimization. Concluding remarks and recommendations for future research directions are presented in Chapter 8.

CHAPTER 2

BACKGROUND

2.1 Introduction to Lamb waves

Of all of the different techniques, damage detection using Lamb waves has shown great promise. Lamb waves are capable of detecting the existence of damage, severity of damage, type of damage, location of damage and size of damage. Lamb waves are elastic waves confined to a plate that can travel long distances. Horace Lamb, an applied mathematician, was the first to describe and analyze these waves [20]. However, they were not used for damage detection until much later by Worlton [21].

Lamb waves are elastic waves that extend throughout the entire thickness of a plate-like structure and thus can be used to detect both internal and surface damage [22]. The time of flight, wave attenuation, phase information and propagation characteristics of Lamb waves change with different types of damage [23] so they provide valuable information about the integrity of a structure. The amplitude ratio of undamaged to damaged response is known to provide information on the severity of damage and the difference in time of flight provides information on the location of damage [24].

Lamb waves have multiple symmetric and anti-symmetric modes. Two fundamental modes, zero order symmetric (S_0) and zero order anti-symmetric mode (A_0), are shown in Figure 2.1. These two modes exist at all frequencies. As the frequency increases, higher order modes are generated and an infinite number of modes exist. Symmetric waves are termed longitudinal waves, or longitudinal modes, and the average displacement is parallel to the wave propagation. Anti-symmetric Lamb waves are termed transverse waves, or flexural

modes, and the average displacement is normal to the wave propagation. An actuator placed on one of the surfaces of a structure generates strong anti-symmetric mode Lamb waves while two co-located actuators placed on top and bottom surfaces, excited in-phase, generate strong symmetric mode Lamb waves in a structure [25].

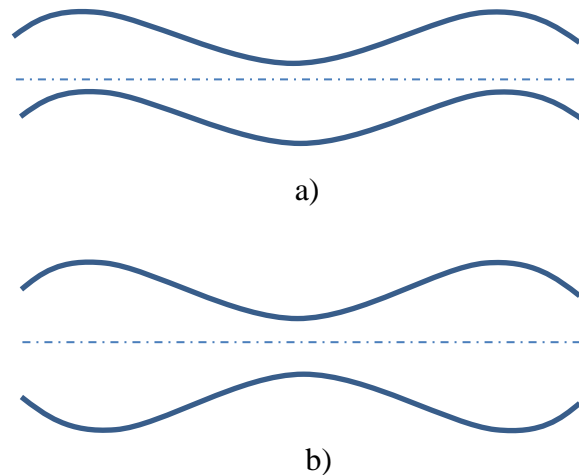


Figure 2.1. Graphical representation of Lamb wave modes: a) anti-symmetric and b) symmetric.

Lamb waves are dispersive in nature; that is, different frequency components of Lamb waves travel at different wave speeds within a solid structure. This makes the study of Lamb wave response challenging. Thus, it is important to keep the Lamb waves less dispersive and excite only the required modes. A careful choice of actuation signal helps in exciting only the zero order modes.

2.2 Lamb wave methods

The use of Lamb waves for damage detection includes two primary modes of operation, pulse echo and pitch catch [26]. In pulse echo, either the same transducer or a sensor co-located with an actuator is used to transmit and receive signals; damage detection relies on the reflections or echoes from any discontinuities present such as edges, cracks, or delamination in a structure. This approach has shown promise in detecting the location of damage by studying the time of flight of the reflections. In pitch catch, a signal transmitted by

an actuator located at one end of a structure is received by a sensor located at the opposite end; in this case, damage detection relies on change in the amplitude ratio and time of flight of the transmitted signal. This approach can cover long distances but requires a dense network of sensors [27].

2.3 Sensing methods

Sensors play an important role in the data acquisition phase in SHM. Over the years, many different sensors have been considered. The different sensors will be described in this section.

Fiber optic sensors (FOS) are small, light weight, corrosion resistant, immune to electromagnetic interference, and can be multiplexed. They possess excellent compatibility with the data transmission network and the signal can be transmitted over a long distance without significant loss [28]. In addition, FOS do not require an electrical connection. However, they are temperature sensitive and highly directional.

Optical sensing using fiber Bragg grating (FBG) sensors are gaining increasing attention in SHM. In a FBG sensor, the period of Bragg grating determines the wavelength of reflected light. Any strain induced in a structure leads to a corresponding change in the grating period of a surface bonded or embedded sensor. This in turn changes the reflected wavelength giving valuable information about the state of a structure. Since FBGs are small and light weight, they are an ideal candidate for embedding in a structure. However, FBGs are brittle in nature and it becomes necessary to encapsulate them. The embedded FBGs can then serve as potential sites for initiation of cracks and delamination [29]. Another challenge is verification of the proper operation of an embedded FBG sensor.

Strain gauges are small, inexpensive, light weight and simple to implement [30]. Strain gauges are essentially resistive foil gauges. They exhibit a change in resistance under mechanical stress or strain. The sensors require a DC voltage to be applied across the gauge

making them susceptible to electromagnetic interference. Similar to FBG, another disadvantage of a strain gauge is that the sensitivity covers a small area and thus a large number of sensors are required for a large structure. This characteristic increases the complexity of any system relying on strain gauges [31]. In addition, the temperature range and fatigue life of strain sensors are somewhat limited.

Magnetostrictive sensors are based on the principle of converting mechanical energy into magnetic energy and vice versa. They are light weight, durable, and can act as both actuators and sensors. For these reasons, they are suitable for active health monitoring [32]. However, they are temperature sensitive, expensive, and several aspects regarding their use are being researched. In addition, embedding magnetostrictive sensors can degrade the quality of a structure.

Piezoelectric transducers are light weight and are sensitive to small amounts of strain. They generate relatively high amplitude output signals compared to other sensors. One of the biggest advantages of lead zirconate titanate (PZT) sensors is the ease with which the sensors can be used in different detection techniques - ultrasonic Lamb waves, acoustic emission, and strain-based methods [16]. In addition, the same PZT transducer can act as either an actuator or a sensor at any time. This allows for baseline-free detection and gives the flexibility to monitor proper sensor operation. Several authors have proposed different methods such as residual measurement and modal factors for validating sensor operation [33, 34]. Given these advancements, in this thesis, piezoelectric transducers coupled with Lamb waves were used for detection of a crack in composite materials.

2.4 Piezoelectric transducers and principle of operation

Surface mounted PZT actuators are commonly used to generate Lamb waves in composite materials [35]. Piezoelectric transducers operate on the principles of both the piezoelectric and the inverse piezoelectric effect. The crystalline property of a piezoelectric

material is such that electrical pulses are converted into mechanical vibrations according to the inverse piezoelectric effect when this material is used as an actuator. A piezoelectric sensor, on the other hand, converts mechanical vibrations into electrical charge by the piezoelectric effect. The IEEE matrix notations [36] for coupled electromechanical effect is given by Equations (2.1) and (2.2).

$$D = \varepsilon^\sigma E + d\sigma \quad (2.1)$$

$$\varepsilon = S^E \sigma + d^T E \quad (2.2)$$

where D is the displacement, E is the electric field vector, ε is the mechanical strain vector, σ is the mechanical stress vector, d is the piezoelectric strain constant, ε^σ is the dielectric permittivity matrix at zero stress and S^E is the elastic compliance matrix at a constant electric field.

Commonly used piezoelectric materials are lead zirconate titanate (PZT), lead titanate (PT), lead metaniobate (PN), and polyvinylidene fluoride (PVDF). PVDF is mechanically flexible although has some limitations. This material can be operated at a maximum temperature of 80°C losing its piezoelectric properties at high temperature. Therefore, PVDF is not a suitable choice for embedding into composite materials that have to be cured at high temperatures. Also PVDF has lower sensitivity and requires higher actuation power than PZT. PZT can withstand operating temperatures as high as 365°C making PZT a more popular choice when using the Lamb wave detection technique [27]. However, PZTs are not mechanically flexible so new piezocomposite materials, such as macro fiber composite (MFC) type P1 and P2 and active fiber composites (AFCs), are under investigation to improve surface conformability.

2.5 Actuation parameters

PZT actuators are excited by application of a voltage. The voltage amplitude, number of cycles, pulse shape, and frequency of actuation for PZT actuators have been investigated

[23, 37]. A higher voltage helps to generate stronger Lamb waves with a larger signal to noise ratio but at the cost of high power consumption [38]. High power consumption is not recommended as SHM systems typically have requirements of low power. A voltage of 5-10 V has been found to be optimum for most SHM applications. A signal with a larger number of peaks has a higher energy associated with it. This aspect helps in long distance propagation as it compensates for any attenuation due to damping. However, increasing the number of peaks increases the pulse width and, in turn, the interference [39, 40]. A three to five cycle Hanning modulated tone burst has been shown to be an optimal form of actuation because this method allows separating the anti-symmetric and symmetric modes and allows separating the reflection from the edges or from cracks [41]. Diamanti and Soutis [42] studied the use of low frequency for composite damage detection. Lower frequencies excite a smaller number of modes making them more distinguishable. The first order anti-symmetric (A_0) mode has a smaller wavelength for a given frequency compared to the first order symmetric (S_0) mode making A_0 waves more sensitive to small levels of damage. In addition, S_0 modes undergo higher attenuation during propagation [24, 40]. Given these characteristics, a five cycle tone burst of 1 kHz center frequency and an amplitude of 6 V to generate A_0 mode Lamb waves was considered in the testing protocol. The excitation input signal is shown in Figure 2.2.

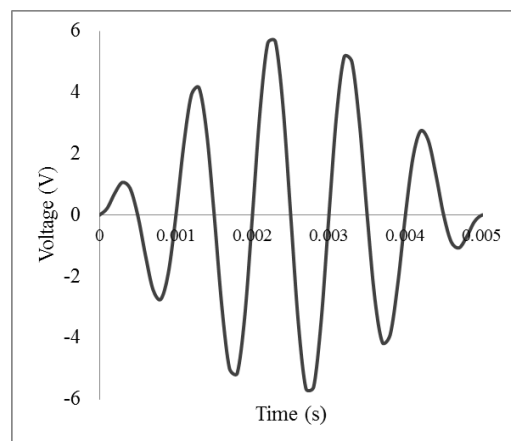


Figure 2.2. A typical PZT excitation input signal for the testing scheme used in this study.

2.6 Transverse crack

In this thesis, the Lamb wave technique was implemented to detect a type of damage observed in composite structures, a transverse crack. Composite materials have lower strength in the transverse direction. A transverse crack in a 90° orientation ply can develop very early in the fatigue cycle [43] and eventually cause other damage such as interlaminar delamination [44]. A transverse fatigue crack also degrades the stiffness and dimensional stability of the composites [45] and can extend throughout the thickness [46]. A reduction in material stiffness is explained by Amara *et al.* using a modified shear lag analysis [47]. Owing to the adverse effects of transverse cracks in composite materials, it becomes important to develop a damage detection system to identify the same. Soni *et al.* [40] used a Lamb wave based approach with PZT actuators and sensors to study the changes in amplitude ratio due to a fatigue crack. However, they conducted their tests on aluminum joints and not on composite materials. El-Kafrawy [48] studied the mode shape and natural frequency changes with a transverse crack in steel beams. In my research, a Lamb wave based approach was used to study a transverse crack in composite materials. The Lamb waves were generated using a surface mounted PZT actuator and the response was measured using a surface mounted PZT sensor. The response of the Lamb waves to both surface transverse cracks of varying depth and to embedded transverse cracks in composite material coupons were studied. In addition, a composite coupon containing a simulated crack was modeled using the commercial finite element software, Abaqus, and was validated using experimental results.

2.7 Finite element analysis

Several authors [48-50] have performed modal analysis of a cantilever beam with a surface crack using numerical methods. The changes in natural frequency and mode shape due to a transverse crack have been investigated. El-Kafrawy found a decrease in natural

frequency with an increase in the crack depth. In that same work, the natural frequency was found to decrease when the location of a crack was moved from the fixed end to the free end.

As mentioned in section 2.1, Lamb waves are dispersive in nature and can be complicated to analyze. The complexity increases for Lamb wave analysis in a composite material because of its orthotropic nature. Finite element analysis helps in simulating Lamb waves in composite materials. Toyoma *et al.* [45] simulated Lamb waves in a composite material and demonstrated the reduction in S_0 mode velocity and stiffness with an increase in transverse crack density. Kessler *et al.* [37] numerically studied the energy change in a composite specimen due to a transverse crack using Lamb waves and piezoelectric actuators and sensors. Extensive research has been performed to numerically model the piezo actuation. The excitation input to the actuator was modeled by giving a suitable x and y displacement [51], by applying a moment load [52], or by applying an out-of-plane force on the surface node at the free end [53]. Soni *et al.* [40] and Jha *et al.* [23] modeled piezo actuation by applying an electric potential to Abaqus three dimensional eight node piezoelectric elements to detect a fatigue crack in an aluminum lug joint and to detect delamination in a composite material, respectively. A good match was found between experimental and modeling results in their work. An approach similar to Soni *et al.* and Jha *et al.* was followed in our research to model piezo actuators for studying a transverse crack in composite materials.

2.8 Finite element analysis for optimization

After verification using experimental data, integration of finite element models and optimization algorithms was implemented that helps in developing a reliable and cost effective damage detection system. An optimized system helps in reducing the power, cost and weight penalties. Another important application of SHM and sensor location optimization is estimating the remaining useful life of a structure by predicting the next possible damage location and the severity of that damage. Optimization algorithms, such as genetic and

evolutionary algorithms [54] and stable noisy optimization by branch and fit (SNOBFIT) [55], are used to optimize the number and location of sensors. In this thesis, interfacing Abaqus simulation and the optimization algorithm will be discussed.

CHAPTER 3

FABRICATION OF COMPOSITE PANEL

Composite materials can be manufactured using resin transfer molding (RTM), vacuum assisted resin transfer molding (VARTM), compression molding, and the filament winding method. In this study, a VARTM process is used to fabricate CFRP composite panels. Composite materials manufactured using the VARTM process have the advantages of improved quality, improved fiber wet-out, reduced void content, and reduced tooling costs compared to RTM [56] and hand layup.

Surface treated and sized unidirectional carbon fibers, IM7, were used for fabricating composite panels. IM7 is a high tensile and shear strength fiber. The VARTM process is comprised of surface mold preparation, fiber layup, vacuum creation, resin preparation, resin infusion and curing. In this thesis, fabrication of a panel with orientation $[0_6/90_4/0_6]_T$ containing a simulated embedded crack is described. The remaining panels required for testing were similarly fabricated. The carbon fiber fabric was cut into $304.8 \text{ mm} \times 304.8 \text{ mm}$ squares that form the 16 plies. Four plies, oriented in the 90° direction, were cut in the middle, parallel to the fiber direction to simulate the transverse crack.

The surface mold was prepared by spraying a release agent, previously cleaned with acetone, to aid in fabric release. In addition to the release agent, a release film was placed on the mold before laying up the fabric. Six plies were laid in the 0° direction, followed by four plies with the pre-fabricated cut in the 90° direction. A thin parafilm was placed along the crack to avoid fiber bonding during fabrication. The remaining six plies were placed on top in the 0° direction. A second release film and distribution mesh was placed above the fabric. A distribution mesh promotes uniform distribution of resin and controls resin flow. The entire

material setup was sealed in a vacuum bag providing an inlet for resin infusion and an outlet for excess resin collection (Figure 3.1). A pressure gauge placed at the outlet monitors the vacuum level. The vacuum assists in driving the resin and in consolidating the fibers to achieve the desired fiber volume fraction [57]. Once a vacuum was created, the system was allowed to debulk for an hour to remove air pockets, to prevent wrinkles, and to promote adhesion.

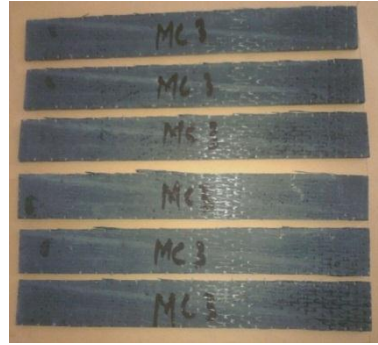
SC780 resin, a two part epoxy mixed in a 4:1 ratio with the hardener, was used as the matrix material. The resin was infused into the panel and left for an additional 1.5 hours to allow complete resin distribution and fiber wet-out. The flow pattern and fill time of resin distribution have been investigated using finite element models by others [58, 59]. It was found that a release film placed between carbon fiber fabric and distribution mesh reduced the resin fill time. The vacuum was removed and after an overnight room temperature cure, the panel was cured in an oven for 6 hours at 71°C, and then 2 hours at 104°C to complete the resin cross-linking step. Some of the stages in composite fabrication are illustrated in Figure 3.1 and 3.2. The final panels were cut into 254 mm × 25.4 mm coupons for damage detection testing and 25.4 mm × 25.4 mm pieces for moisture and acid digestion testing. The fiber volume fractions of the fabricated composite panels were found to be in the range of 48-50%.



Figure 3.1. Two photographs to illustrate composite panel fabrication stages: a) fabric layup and b) resin infusion



a)



b)

Figure 3.2. Two photographs to illustrate composite panel fabrication stages: a) the final cured composite panel and b) coupons trimmed from the composite panel.

CHAPTER 4

EXPERIMENTAL ANALYSIS

The experimental results from the damage detection tests are presented in this chapter. The tests were performed on 254 mm × 25.4 mm coupons machined from 304.8 mm × 304.8 mm panels, both undamaged and those with simulated damage. A Lamb wave based approach was used for damage detection. A surface mounted PZT actuator was used to excite Lamb waves in a composite coupon and the response was received by a surface mounted PZT sensor. The response from an undamaged composite coupon was used to provide a baseline for reference.

4.1 Data acquisition setup

The composite coupon was fixed at one end with a PZT actuator surface-mounted on the free end. An AC signal applied to the terminals of a PZT actuator puts the coupon into vibrations by the inverse piezoelectric effect. A Hanning modulated five cycle tone burst signal at a center frequency of 1 kHz was used for Lamb wave excitation. The actuation signal was amplified by a factor of 20 using a piezo amplifier before sending to the actuator. The Lamb waves, generated by the actuator, were received by the sensor located 60 mm from the clamped end. The sensor generates a voltage equivalent to the induced strain by the direct piezoelectric effect. The sensor was connected to a data acquisition (DAQ) card through a connector box with a sampling rate of 100 kHz. National Instruments LabVIEW software was used to synchronize the actuation initiation (waveform generator) and sensor data collection (DAQ). Real time sensor data were collected for further analysis. The experimental setup is shown in Figure 4.1.

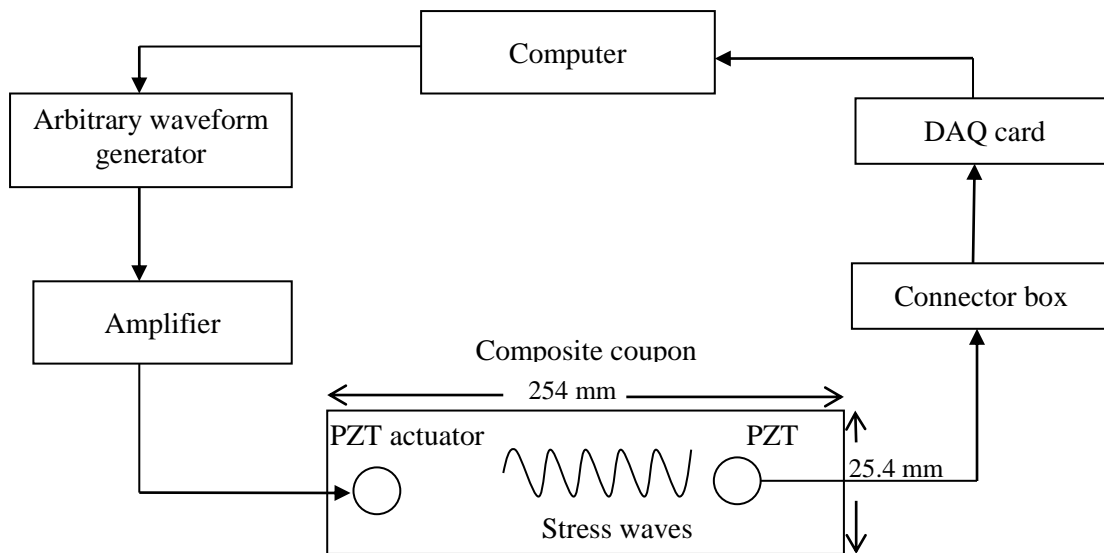


Figure 4.1. Data acquisition system using PZT actuators and sensors.

An Agilent 33210A arbitrary waveform generator was used to generate the actuation input. A National Instruments LabVIEW program was developed using the Agilent 33XXX driver and VIs (virtual instruments) to control the waveform generator through the general purpose interface bus (GPIB) port. A GPIB to USB cable connects the waveform generator to the computer. The arbitrary waveform generation feature was utilized to generate a Hanning burst. The frequency, amplitude, burst count and burst rate of actuation input were user configurable in the LabVIEW program.

The output of the waveform generator was fed to a piezo amplifier AA 301HS that had an amplification factor of 20. The amplitude of the waveform generator was set to $6 V_{p-p}$ to generate an input actuation amplitude of $120 V_{p-p}$ after amplification. This was within a safe margin for the PZT actuator that had an operating range of $180 V_{p-p}$.

Data from PZT sensors were read into a LabVIEW program using the NI DAQmx driver software. The number of sensors to import and the number of samples to read were configurable in the LabVIEW program. The program displayed a real time waveform of voltage versus time for all of the sensors for rapid data analysis. The sensor data was stored in text files for further data analysis.

This experimental system was found to generate the desired amplitude and desired shape A_0 mode Lamb waves in a composite coupon required for this study.

4.2 Test for damage detection

4.2.1 Simulated damage using drilled holes in a laminate

A rectangular PZT actuator (38.1 mm \times 12.7 mm \times 2.54 mm) and a center frequency of 350 Hz was chosen for the preliminary test to detect the presence of a hole. Low frequency PZT actuators and sensors were selected to match the resonant frequency of a 254 mm \times 25.4 mm IM7/SC780 composite coupon. Damage was introduced by drilling holes of varying diameters at the center of a test coupon. A three cycle sine burst with a center frequency of 100 Hz was used for actuation. The coupon was placed on styrofoam to simulate the free-free condition. A PZT actuator was surface mounted at one end of a coupon and a PZT sensor was surface mounted 60 mm from the opposite end as shown in Figure 4.2. The sensor was placed some distance from the end to avoid excessive reflections from the free edge.

Tests were performed on an undamaged coupon to obtain a baseline for reference. Holes with the following diameters: 1.58 mm, 1.98 mm, and 3.175 mm were introduced into the coupon and the data was recorded after each increase in hole size. The results from this test are shown in Figure 4.3.

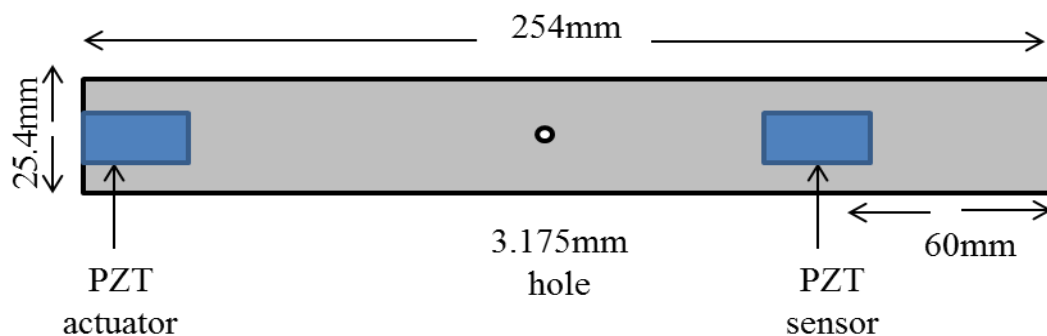


Figure 4.2. A pictorial representation of a damaged composite coupon illustrating the actuator and sensor placement.

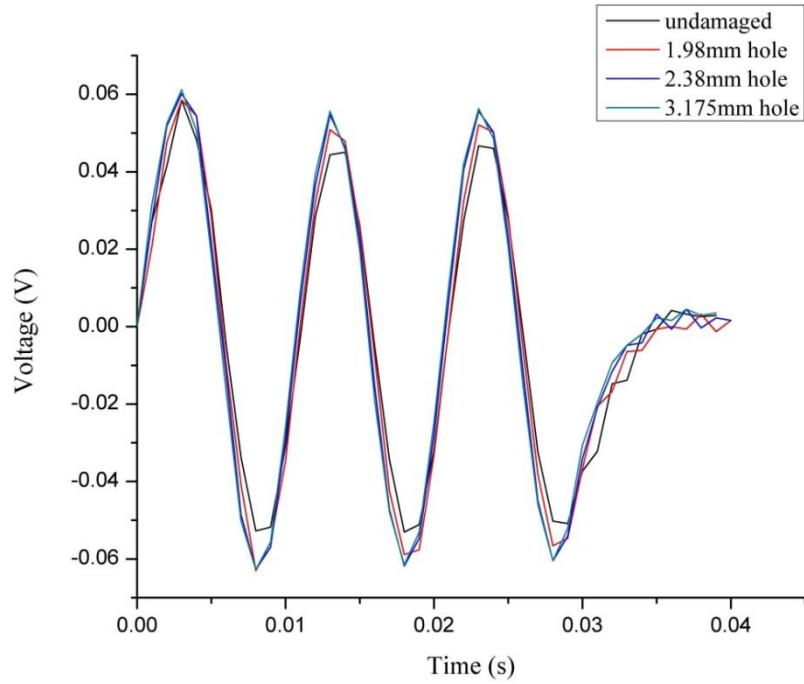


Figure 4.3. Experimental test results comparing the Lamb wave response of an undamaged coupon and coupons with varying hole size.

Another set of tests were conducted to investigate a coupon with a variable number of holes (1-4) at a fixed diameter of 3.175 mm. The holes were placed 20 mm apart as shown in Figure 4.4. Sensor output was measured after the addition of each hole and the results are shown in Figure 4.5.

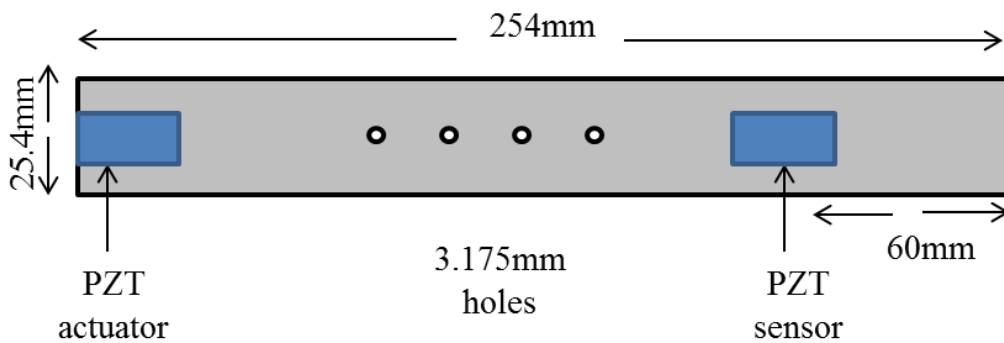


Figure 4.4. A pictorial representation of a composite coupon with four 3.175 mm diameter holes illustrating the actuator and sensor placement relative to the holes.

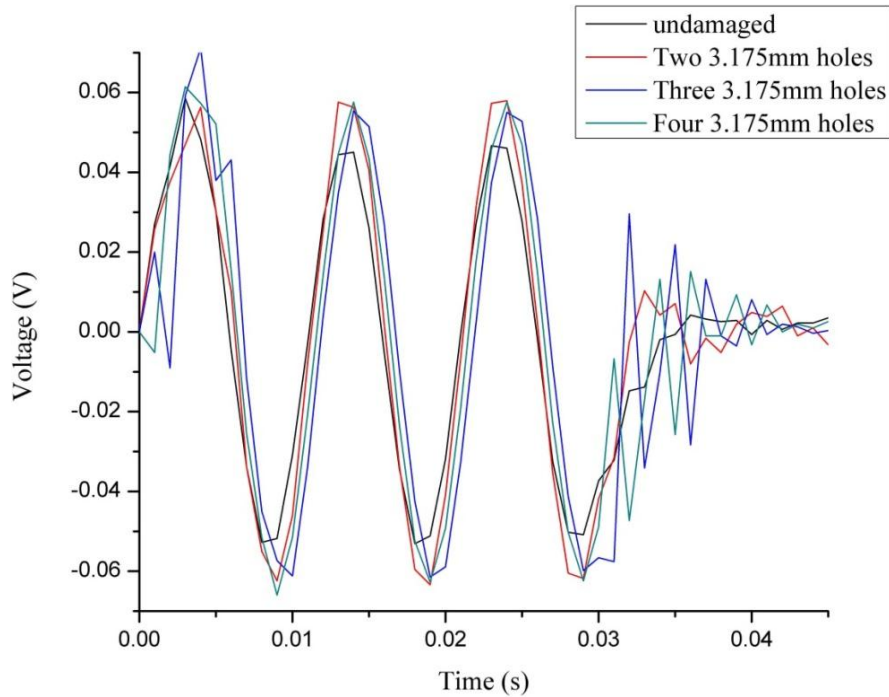


Figure 4.5. Experimental test results comparing the Lamb wave response of an undamaged coupon and coupons with varying number of holes.

From Figure 4.3 and Figure 4.5, we observe that the amplitude ratio of a damaged coupon is higher than an undamaged coupon for both varying hole size and for a varying number of holes. In addition, perturbations were observed in the sensor response for the damaged coupon. Both observations were attributed to reflections from the hole.

4.2.2 Simulated damage using a fabricated transverse surface crack

Tests were performed on 254 mm \times 25.4 mm composite coupons machined from a $[0_{16}]_T$ undamaged panel and a panel with a surface crack in the first four plies transverse to fiber direction. The damaged panel was fabricated using the procedure described in Chapter 3. The response from an undamaged composite coupon was used to provide a baseline for reference. The coupon was clamped at one end with a PZT actuator disk surface mounted on the opposite end. The PZT actuator disk of center frequency 7.3 kHz measured 12.7 mm in diameter and was 0.38 mm thick. A hanning modulated five cycle tone burst signal at a center frequency of 1 kHz was used for Lamb wave excitation. The Lamb waves, generated by the

actuator, were received by a PZT sensor located 60 mm from the clamped end as shown in Figure 4.6.

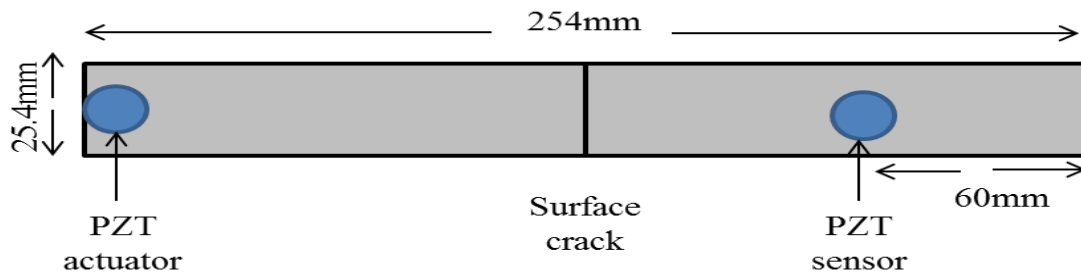


Figure 4.6. A pictorial representation of a composite coupon with a surface crack demonstrating the actuator and sensor placement relative to the crack.

The results from this experiment, comparing the Lamb wave response of an undamaged composite coupon and a coupon with a surface crack, is shown in Figure 4.7. The amplitude ratio of the incident wave for an undamaged coupon was slightly higher than a damaged coupon but the reflections were increased for the damaged coupon compared to the undamaged coupon; this is believed to be due to the presence of the crack.

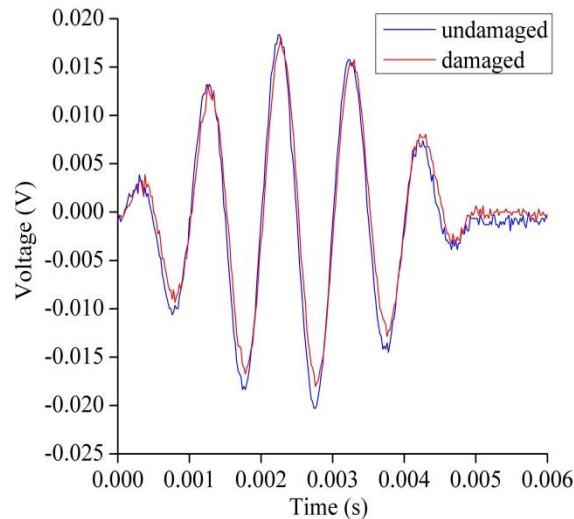


Figure 4.7. Experimental results comparing the Lamb wave response of a $[0_{16}]_T$ orientation undamaged coupon and a coupon with a surface crack in the first four plies.

4.2.3 Simulated damage using a fabricated transverse embedded crack

Tests were performed on 254 mm \times 25.4 mm coupons machined from $[0_{16}]_T$ and $[0_6/90_4/0_6]_T$ undamaged panels as well as the panels with a simulated crack. The crack location is at the midspan of the specimen in the middle four plies, extending through the

width. The composite coupons were fabricated using the procedure described in Chapter 3. The experimental setup is shown in Figure 4.8.

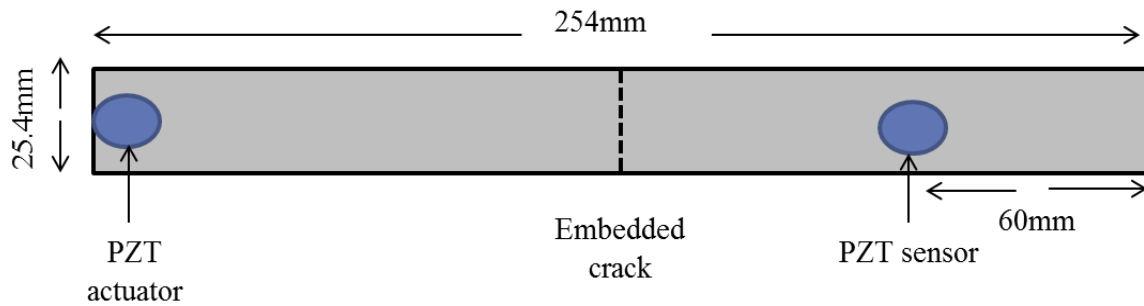


Figure 4.8. A pictorial representation of a composite coupon with an embedded crack demonstrating the actuator and sensor placement relative to the crack.

Figure 4.9 shows the comparison between an undamaged composite coupon and a coupon with a simulated crack for both $[0_{16}]_T$ and $[0_6/90_4/0_6]_T$ composites. Less than 1% difference was observed between an undamaged coupon and a coupon with an embedded crack for both orientation cases. Amplitude ratio and time of flight for both undamaged and damaged coupons were found to be essentially the same. The response of the damaged coupon was essentially identical to the undamaged coupon response.

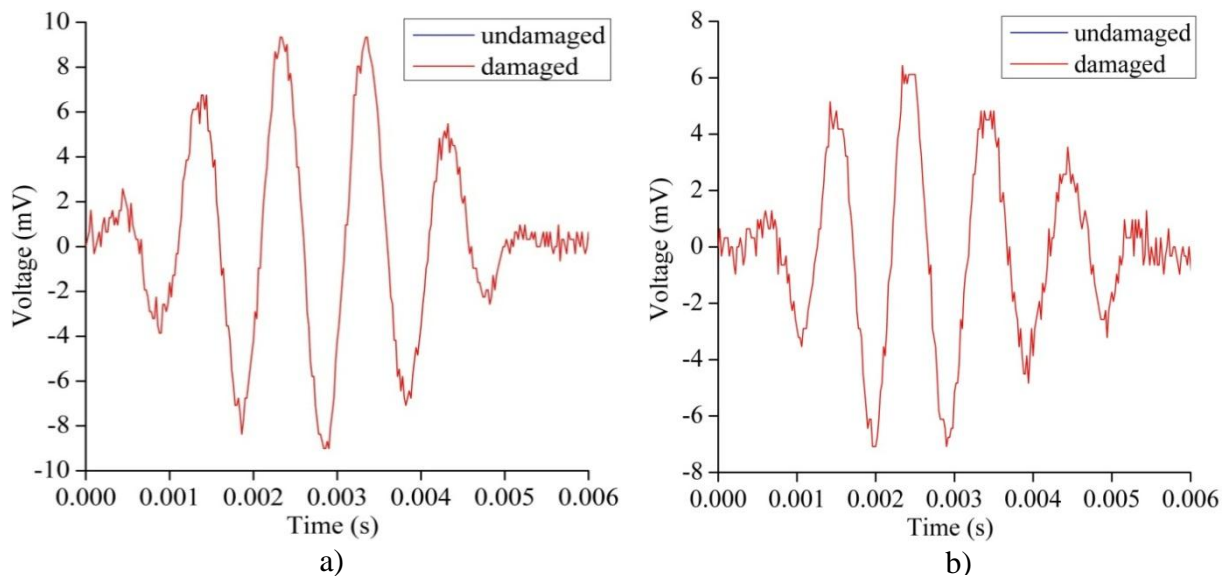


Figure 4.9. Experimental results comparing the Lamb wave response of an undamaged coupon and a coupon with an embedded crack for: a) a $[0_{16}]_T$ composite coupon and b) a $[0_6/90_4/0_6]_T$ composite coupon.

CHAPTER 5

FINITE ELEMENT ANALYSIS

A three dimensional finite element analysis was carried out using Abaqus (version 6.10), a commercial FEM software, to study the Lamb wave response of a composite test coupon. Three dimensional eight node solid brick elements were used to discretize both an undamaged coupon and a coupon with a simulated crack. Abaqus benchmark tests were performed to determine the ideal method to model a crack in a composite and to determine the optimum mesh size for dynamic analysis.

5.1 Composite benchmark test

In Abaqus, composite materials can be modeled using one of the following types of elements:

- Four node conventional shell elements (S4R)
- Eight node continuum shell elements (SC8R)
- Eight node linear brick elements (C3D8R)
- Twenty node quadratic brick elements (C3D20R)

An appropriate element type for composite modeling was chosen by performing three different types of tests: a pull test on a $[0/45/-45/90]_s$ laminate; a deflection test on a specially orthotropic symmetric $[0/90/0/90]_s$ laminate; and a deflection test on an off-axis symmetric $[-56/-25/-38/-35]_s$ laminate. The composite material properties used for benchmarking tests are given in Table 5.1 [60].

Table 5.1. Material properties of IM7/PETI5 composite used for benchmarking tests [60].

| E_{11} | E_{22} | E_{33} | G_{12} | G_{13} | G_{23} | ν_{12} | ν_{13} | ν_{23} | α_1 | α_2 |
|----------|----------|----------|----------|----------|----------|------------|------------|------------|-----------------------------------|------------|
| Msi | | | | | | | | | $\times 10^{-6}/^{\circ}\text{F}$ | |
| 24.2 | 1.28 | 1.28 | 0.73 | 0.73 | 0.48 | 0.3 | 0.3 | 0.34 | -0.722 | 10.8 |

Table 5.2. Material properties of IM7/PETI5 composite used for benchmarking tests (re-written using SI units).

| E_{11} | E_{22} | E_{33} | G_{12} | G_{13} | G_{23} | ν_{12} | ν_{13} | ν_{23} | α_1 | α_2 |
|----------|----------|----------|----------|----------|----------|------------|------------|------------|-----------------------------------|------------|
| GPa | | | | | | | | | $\times 10^{-8}/^{\circ}\text{K}$ | |
| 166.8 | 8.824 | 8.824 | 5.032 | 5.032 | 3.309 | 0.3 | 0.3 | 0.34 | -0.282 | 4.22 |

The pull test was performed on a $[0/45/-45/90]_s$ composite coupon, simply supported on three sides of the coupon, and subjected to an axial displacement load of 2 mm on the fourth side as shown in Figure 5.1. The composite coupon was meshed with 600 elements. The test was repeated for the four different types of elements under consideration. A sample von Mises stress result for a composite coupon meshed with S4R elements is shown in Figure 5.2.

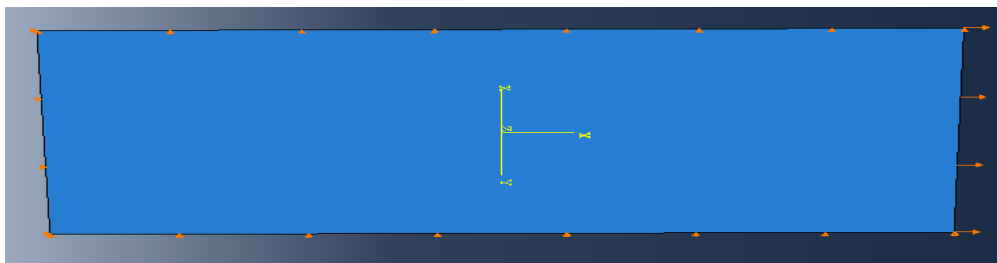


Figure 5.1. FE model of a composite coupon representing the load and boundary conditions for a pull test.

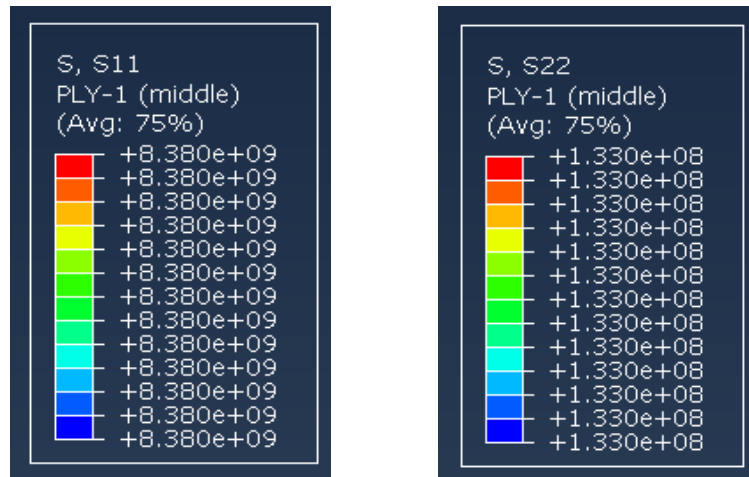


Figure 5.2. Abaqus results showing the von Mises stress contour legends of the longitudinal and transverse stresses (in Pa) for a composite coupon modeled with S4R elements under an axial displacement load.

The exact solution for the pull test was calculated using classical lamination theory (CLT). Longitudinal, transverse and shear stress results for composite coupons modeled with four different types of elements were compared to the exact solution. The percentage error was calculated for each of the cases to report deviations from the exact solution. The results are tabulated in Table 5.3.

Table 5.3. Comparison of the exact solution and the Abaqus solution for von Mises longitudinal, transverse and shear stresses for different types of elements.

| | σ_x (Pa) | % error | σ_y (Pa) | % error | τ_{xy} (Pa) | % error |
|----------------------|-----------------|---------|-----------------|---------|------------------|---------|
| 0 orientation plies | | | | | | |
| CLT | 8.38E+09 | | 1.33E+08 | | 0.00E+00 | |
| Abaqus - SC8R | 8.38E+09 | 0.00 | 1.33E+08 | 0.00 | 0.00E+00 | 0.00 |
| Abaqus - S4R | 8.38E+09 | 0.00 | 1.33E+08 | 0.00 | 0.00E+00 | 0.00 |
| Abaqus - C3D8R | 8.39E+09 | 0.07 | 1.38E+08 | 3.76 | 0.00E+00 | 0.00 |
| Abaqus - C3D20R | 8.38E+09 | 0.00 | 1.33E+08 | 0.00 | 0.00E+00 | 0.00 |
| 45 orientation plies | | | | | | |
| CLT | 2.54E+09 | | 2.03E+09 | | 1.98E+09 | |
| Abaqus - SC8R | 2.53E+09 | 0.39 | 2.02E+09 | 0.44 | 1.98E+09 | 0.00 |
| Abaqus - S4R | 2.53E+09 | 0.39 | 2.02E+09 | 0.44 | 1.98E+09 | 0.00 |
| Abaqus - C3D8R | 2.524E+09 | 0.63 | 2.02E+08 | 0.44 | 1.98E+09 | 0.00 |
| Abaqus - C3D20R | 2.524E+09 | 0.63 | 2.02E+08 | 0.44 | 1.98E+09 | 0.00 |
| 90 orientation plies | | | | | | |
| CLT | 4.43E+08 | | 1.33E+08 | | 0.00E+00 | |
| Abaqus - SC8R | 4.43E+08 | 0.00 | 1.33E+08 | 0.00 | 0.00E+00 | 0.00 |
| Abaqus - S4R | 4.43E+08 | 0.00 | 1.33E+08 | 0.00 | 0.00E+00 | 0.00 |
| Abaqus - C3D8R | 4.38E+08 | 1.13 | 1.27E+08 | 4.44 | 0.00E+00 | 0.00 |
| Abaqus - C3D20R | 4.41E+08 | 0.50 | 1.30E+08 | 1.95 | 0.00E+00 | 0.00 |

Transverse deflection tests were performed on a 40 m × 40 m × 0.8 m, [0/90/0/90]_s composite plate subjected to a uniform pressure of 10⁶ N/m² on the top surface. The composite plate was simply supported on all four edges. The load and boundary conditions for a two dimensional shell composite plate are shown in Figure 5.3 while the load and boundary conditions for a three dimensional brick composite plate are shown in Figure 5.5.

The test was repeated for the four elements under consideration. The composite plate was discretized using 1600 elements of type S4R, 1600 elements of type SC8R, 80000 elements of type C3D8R and 20000 elements of type C3D20R in each of the four cases. A similar set of tests were performed on an off-axis symmetric $[-56/-25/-38/-35]_s$ orientation composite plate. The resultant deflection contour plots for a composite plate meshed using shell and brick elements are shown in Figure 5.4 and Figure 5.6.

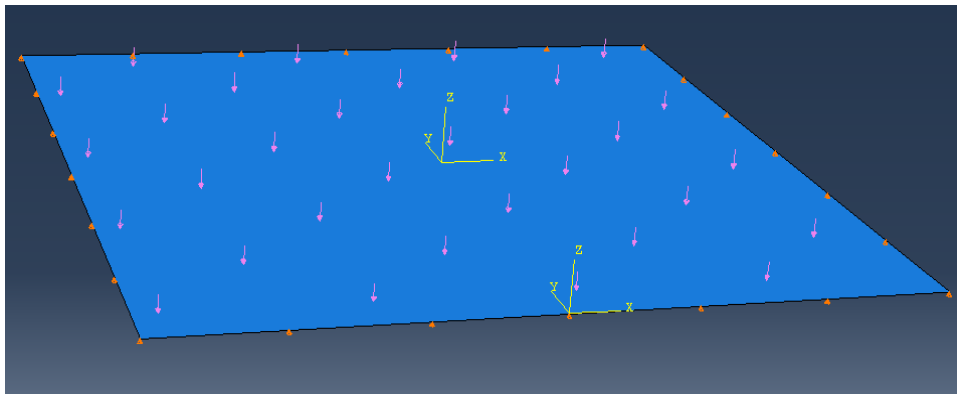


Figure 5.3. FE model of a composite plate meshed with 2D shell elements representing the load and boundary conditions.

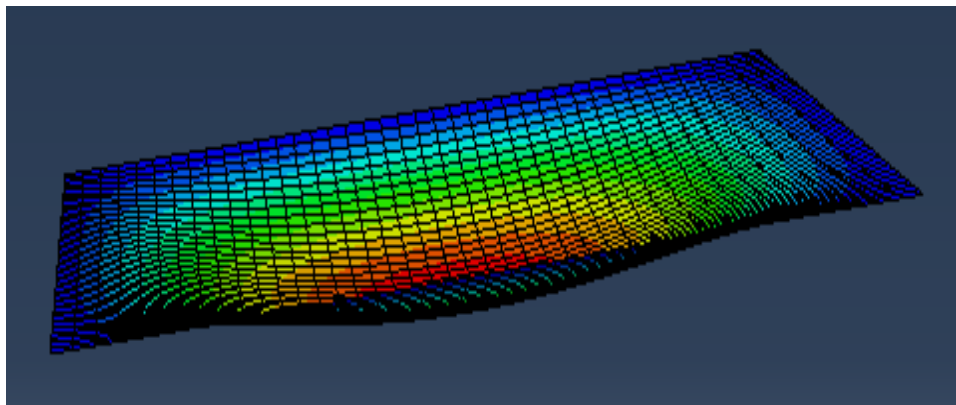


Figure 5.4. Abaqus results showing the deflection contour plot for a 2D shell composite plate under uniform transverse pressure load.

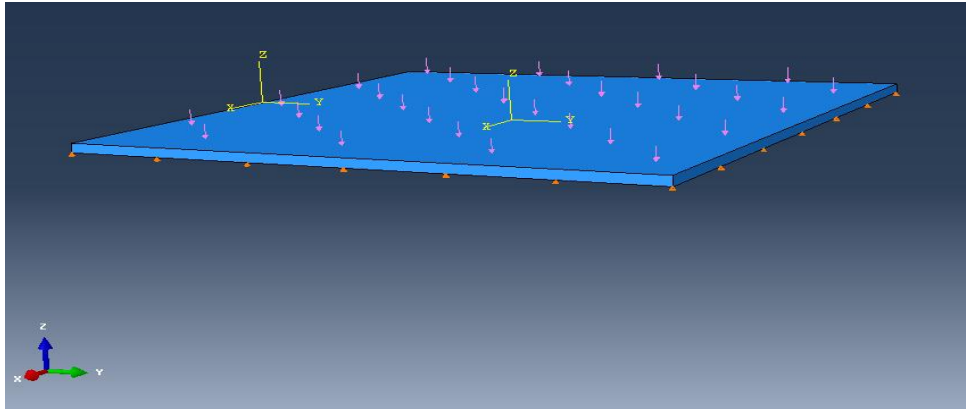


Figure 5.5. FE model of a composite plate meshed with 3D brick elements representing the load and boundary conditions.

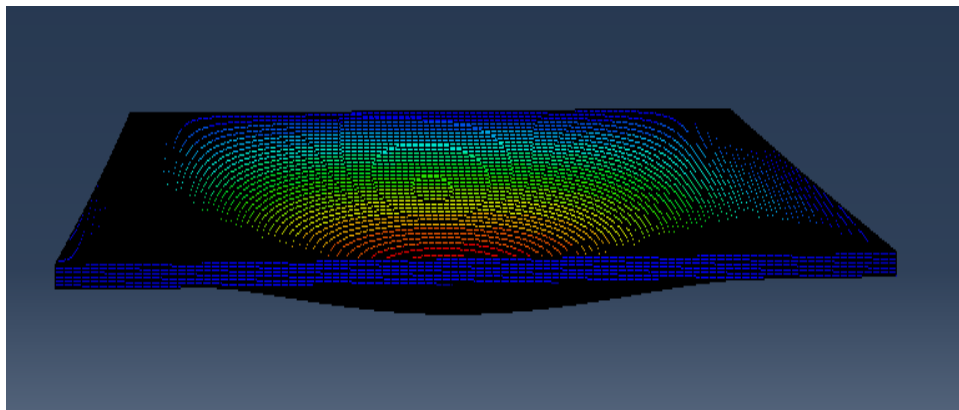


Figure 5.6. Abaqus results showing the deflection contour plot for a 3D brick composite plate under uniform transverse pressure load.

Deflection results for both cases were determined using classical laminated plate theory. The Abaqus results from both of the deflection tests for the four types of elements under consideration were compared to the exact solution. The percentage error was calculated for each of the cases to report deviations from the exact solution. The results are tabulated in Table 5.4 and Table 5.5.

Table 5.4. Comparison of the exact solution and the Abaqus solution for deflection observed in a specially orthotropic symmetric composite plate for different types of elements.

| Deflection results in m | Co-ordinate (20,20) | %error | Co-ordinate (1,1) | %error | Co-ordinate (10,10) | %error |
|-------------------------|---------------------|--------|-------------------|--------|---------------------|--------|
| Exact solution | 4.85837 | | 0.03344874 | | 2.5203352 | |
| Abaqus - SC8R | 4.933 | 1.53 | 0.0369938 | 10.59 | 2.56765 | 1.87 |
| Abaqus - S4R | 4.932 | 1.51 | 0.0345508 | 3.29 | 2.56418 | 1.73 |
| Abaqus - C3D8R | 4.939 | 1.65 | 0.034478 | 3.07 | 2.56117 | 1.62 |
| Abaqus - C3D20R | 4.941 | 1.7 | 0.03701 | 10.64 | 2.568 | 1.89 |

Table 5.5. Comparison of the exact solution and the Abaqus solution for deflection observed in an off-axis symmetric composite plate for different types of elements.

| | | Mid-point deflection in m | % error |
|-----------------|----------------|---------------------------|---------|
| Exact solution | | 6.6609 | |
| Abaqus - SC8R | | 6.968 | 4.61 |
| Abaqus - S4R | | 6.973 | 4.69 |
| Abaqus - C3D8R | 20000 elements | 6.064 | 8.96 |
| | 25992 elements | 6.378 | 4.25 |
| | 35912 elements | 6.645 | 0.24 |
| | 80000 elements | 6.961 | 4.51 |
| Abaqus - C3D20R | 12800 elements | 7.01 | 5.24 |
| | 20000 elements | 7.014 | 5.30 |

From Table 5.3, Table 5.4, and Table 5.5, we can see that all four types of elements show very small deviation from the exact solution and model the composite material fairly well. However, eight node brick elements (C3D8R) converge to the exact solution with mesh refinement. In addition, C3D8R elements are more effective when transverse shear and

interlaminar stresses are dominant. Given these characteristics, eight node linear brick elements were used to model composite materials in all of the subsequent exercises.

5.2 Dynamic simulation benchmark tests

Dynamic simulation benchmark testing was performed on an isotropic material to determine the minimum mesh size required for modeling a composite coupon under dynamic load. An aluminum beam, 304.8 mm × 25.4 mm × 5.08 mm, was modeled using eight node linear brick elements. The beam was subjected to a dynamic concentrated force load of $P(t) = 4\sin(150t)$. The material properties used in this test are given in Table 5.6. The number of elements through the thickness was varied from two to eight to optimize the mesh generation.

Table 5.6. Material properties of aluminum for the dynamic simulation test.

| Young's modulus (GPa) | Poisson's ratio |
|-----------------------|-----------------|
| 70 | 0.3 |

The dynamic transverse load was applied at the center of an aluminum beam that was supported on rollers on either end as shown in Figure 5.7. A node at the center of one of the ends was fixed in all three directions. A sample deflection contour plot and corresponding legend for an aluminum beam meshed with two elements through the thickness and subjected to a dynamic load is shown in Figure 5.8.

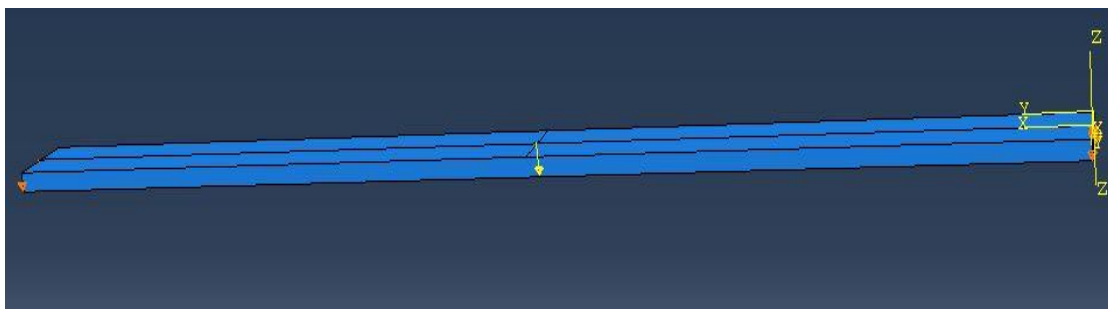


Figure 5.7. 3D FE model of an aluminum beam representing load and boundary conditions for the dynamic simulation test.

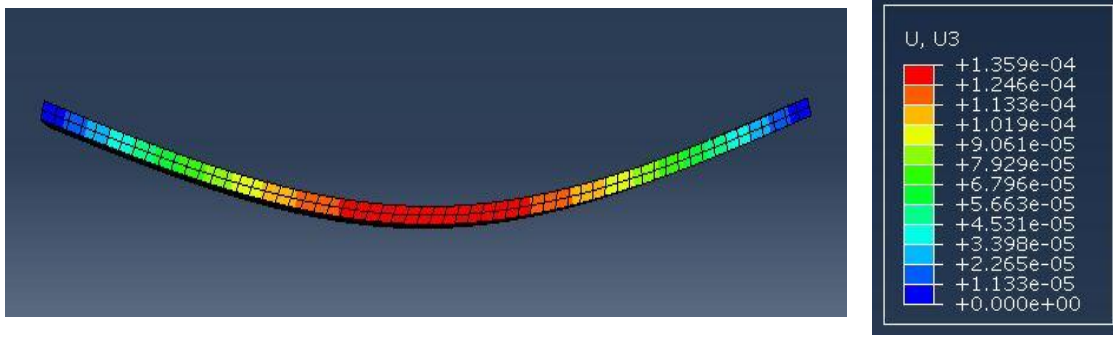


Figure 5.8. Abaqus results showing the deflection contour plot and legend for the dynamic simulation test in m.

For a simply supported beam of length L and constant bending stiffness, subjected to a dynamic load $P(t) = P_0 \sin(\omega t)$, the theoretical deflection value is given by Equation (5.1) and Equation (5.2) [61].

$$w(x, t) = \frac{2P_0 L^3}{\pi^4 EI} \sum_{n=1}^{\infty} \frac{\sin\left(\frac{n\pi a}{L}\right) \sin\left(\frac{n\pi x}{L}\right)}{n^2 - \left(\frac{\omega}{\omega_1}\right)^2} \left[\sin(\omega t) - \left(\frac{\omega}{n^2 \omega_1}\right) \sin(n^2 \omega_1 t) \right] \quad (5.1)$$

where

$$\omega_1 = \frac{\pi^2}{L^2} \sqrt{\frac{EI}{\rho A}},$$

ρ is the density, A is the cross sectional area, I is the area moment of inertia, E is Young's modulus, ω_1 is the first characteristic frequency of vibration, L is the length of the beam, and $a = L/2$.

A MATLAB program was developed to calculate the theoretical deflection at the center of a beam, $a = L/2$. The theoretical results were compared to the Abaqus results obtained from FE models meshed with 2, 4, and 8 elements through the thickness and the corresponding graphs are presented in Figure 5.9, Figure 5.10 and Figure 5.11.

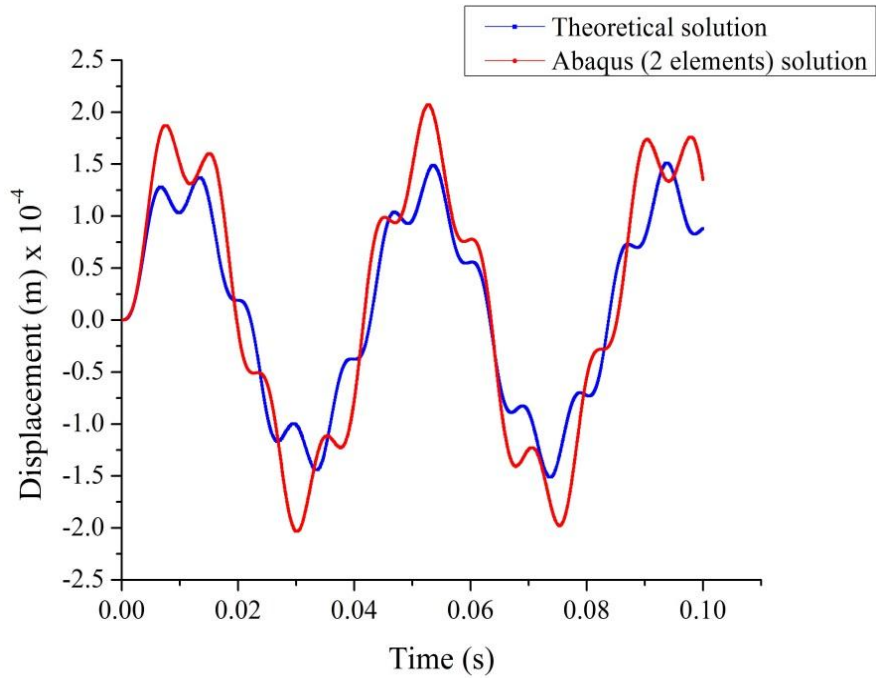


Figure 5.9. Comparison of exact deflection solution and Abaqus solution for an aluminum beam meshed with 2 elements and subjected to a dynamic load.

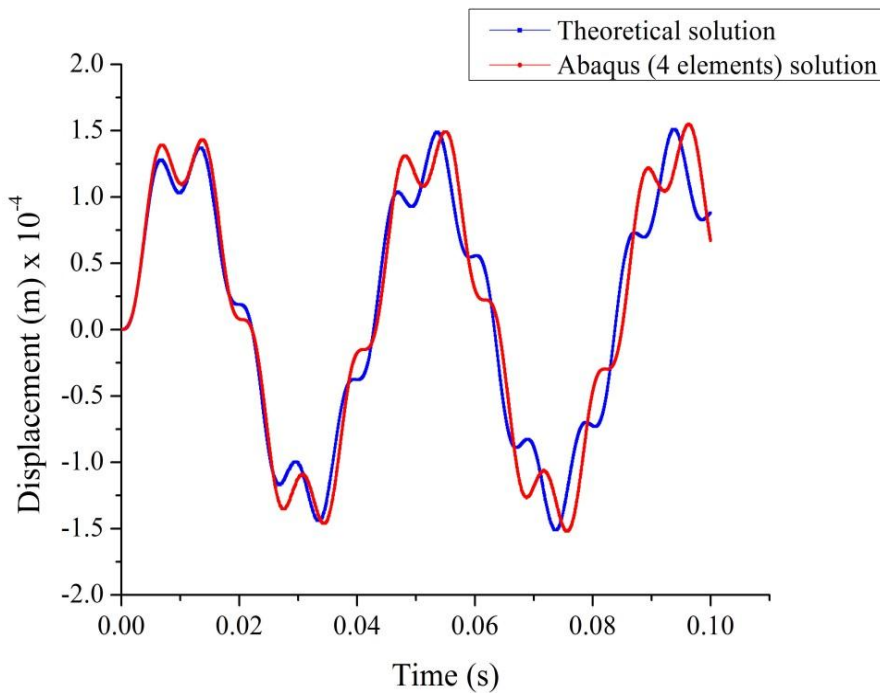


Figure 5.10. Comparison of exact deflection solution and Abaqus solution for an aluminum beam meshed with 4 elements and subjected to a dynamic load.

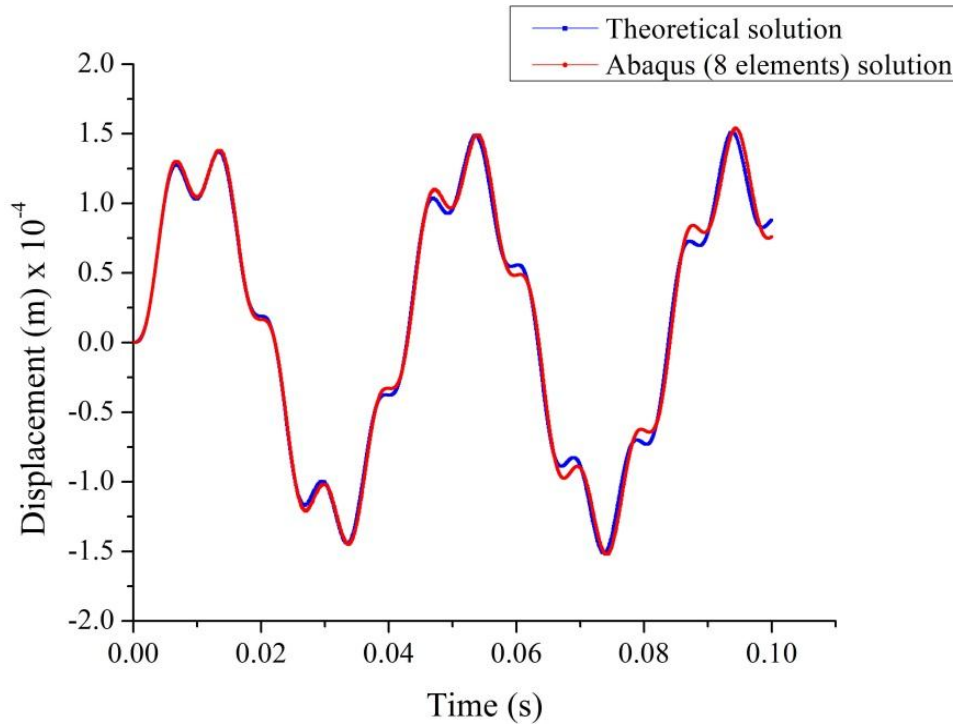


Figure 5.11. Comparison of exact deflection solution and Abaqus solution for an aluminum beam meshed with 8 elements and subjected to a dynamic load.

From Figure 5.9, Figure 5.10 and Figure 5.11, we observe that Abaqus results for a beam meshed with 8 elements through the thickness produced the best match with theoretical results. A minimum of 8 elements through the thickness would thus be used for all further modeling work.

5.3 Crack modeling benchmark tests

A 254 mm × 25.4 mm IM7/SC780 composite coupon was modeled using three dimensional eight node linear brick elements (C3D8R). The stacking sequence for the composite coupon was $[0_{16}]_T$. The damaged composite coupon was modeled with a crack in the middle four plies extending through the width. The material properties used in this model are listed in Table 5.7 and were determined by performing experimental material characterization tests.

Table 5.7. Material properties of the IM7/SC780 composite coupon.

| E1 (Gpa) | E2 (Gpa) | G12 (Gpa) | v | X _t (Gpa) | Y _t (Gpa) |
|----------|----------|-----------|-------|----------------------|----------------------|
| 113.633 | 5.239 | 31.781 | 0.354 | 1.132 | 0.025 |

The crack in the composite coupon was modeled in FEA by creating duplicate overlapping nodes that were free to move apart. A seam crack was assigned at the center for the middle four plies and was extruded through the width to simulate a crack. The crack opening in a composite coupon subjected to an axial tensile load is shown in Figure 5.12. The axial load was applied to verify the model by comparing Abaqus results to theoretical linear elastic shear lag analysis results. Shear lag analysis gives an estimate of the crack density and axial stresses in cracked and remaining plies under thermal and mechanical loads, and has been successfully used by others to analyze a transverse crack [44, 62]. The formulae for stresses based on shear lag analysis are given by Equations (5.3) and (5.4) [63].

$$\sigma_c = \frac{Ka_c}{2\rho^2} \left[\left(\frac{a_r E_r + a_c E_c}{a_r E_r E_0} \right) \sigma_a - (\alpha_c - \alpha_r) \Delta T \right] \left[1 - \frac{\cosh\left(\frac{2\rho x}{a_c}\right)}{\cosh\left(\frac{2\rho h}{a_c}\right)} \right] \quad (5.3)$$

$$\sigma_r = \frac{\sigma_a a_0 - \sigma_c a_c}{a_r} \quad (5.4)$$

where σ_c , σ_r and σ_a are the stresses in the cracked plies, the remaining plies and the entire laminate, respectively, a_c and a_r are the heights of the cracked and the remaining plies, respectively, a_0 is the total height, h is the crack spacing, E_c and E_r are the effective moduli of the cracked and the remaining plies, respectively, E_0 is the average modulus, K is the effective shear stiffness co-efficient, α_c and α_r are the co-efficients of thermal expansion for the cracked and the remaining plies, respectively, ΔT is the temperature difference, and ρ is the density of the composite coupon.

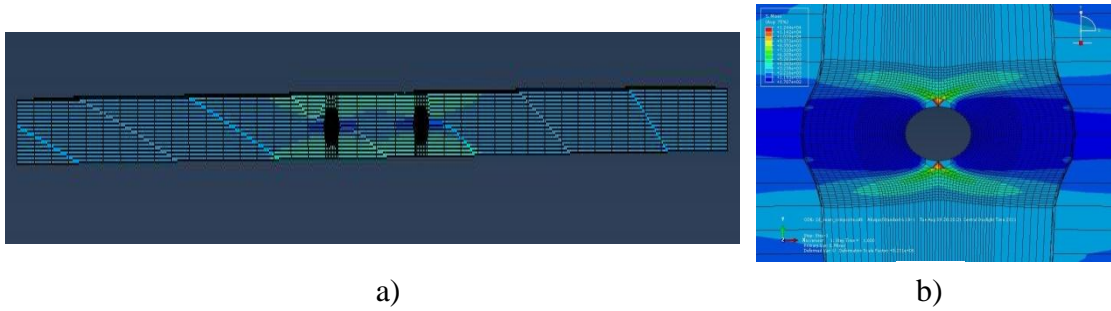


Figure 5.12. a) Abaqus stress contour plot for a composite coupon with two cracks under an axial load and b) an enlarged and exaggerated view near the crack showing the crack opening.

Comparison of Abaqus results and shear lag analysis results for a $[0_{16}]_T$ composite coupon with two transverse cracks is shown in Figure 5.13. Shear lag model results are close to the Abaqus model results with less than 5% error. However, it should be noted that shear lag analysis does not address the stress singularity at the crack tip and hence an exact match is not expected. This confirms the reliability of crack modeling using the Abaqus seam crack feature.

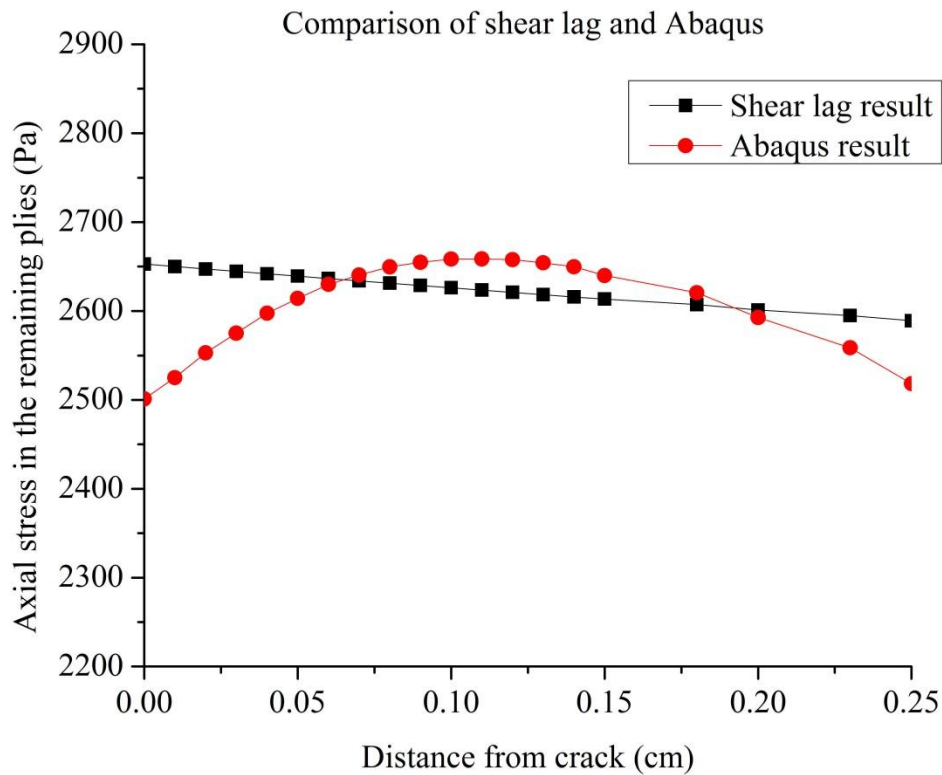


Figure 5.13. Comparison of shear lag model and Abaqus model results for a composite coupon with two transverse cracks.

5.4 PZT modeling

The PZT actuator was modeled using three dimensional eight node piezoelectric elements (C3D8E). The actual PZT actuator disk measured 12.7 mm in diameter and was 0.38 mm thick. The material properties of the PZT are given in Figure 5.14. For modeling convenience, the PZT actuator was modeled using rectangular elements keeping the contact area and thickness intact. Tie constraints were used to bond the composite coupon and PZT actuator. The composite coupon was clamped at one end with the PZT actuator surface mounted on the opposite end. A five cycle tone burst potential of center frequency 1 kHz was applied to the PZT actuator to generate lamb waves in composite coupons.

Stiffness matrix

$$\begin{bmatrix} C_{11} & C_{12} & C_{13} & 0 & 0 & 0 \\ C_{12} & C_{11} & C_{13} & 0 & 0 & 0 \\ C_{13} & C_{13} & C_{13} & 0 & 0 & 0 \\ 0 & 0 & 0 & C_{44} & 0 & 0 \\ 0 & 0 & 0 & 0 & C_{55} & 0 \\ 0 & 0 & 0 & 0 & 0 & C_{66} \end{bmatrix} = \begin{bmatrix} 15.2 & 10.2 & 10.0 & 0 & 0 & 0 \\ 10.2 & 15.2 & 10.0 & 0 & 0 & 0 \\ 10.0 & 10.0 & 12.7 & 0 & 0 & 0 \\ 0 & 0 & 0 & 2.1 & 0 & 0 \\ 0 & 0 & 0 & 0 & 2.1 & 0 \\ 0 & 0 & 0 & 0 & 0 & 2.5 \end{bmatrix} 10^{10} N/m^2$$

Dielectric constant

$$\begin{bmatrix} \epsilon_{11} & 0 & 0 \\ 0 & \epsilon_{11} & 0 \\ 0 & 0 & \epsilon_{33} \end{bmatrix} = \begin{bmatrix} 1780 & 0 & 0 \\ 0 & 1780 & 0 \\ 0 & 0 & 1950 \end{bmatrix}$$

Piezoelectric constant

$$\begin{bmatrix} 0 & 0 & 0 & 0 & d_{15} & 0 \\ 0 & 0 & 0 & d_{24} & 0 & 0 \\ d_{31} & d_{31} & d_{33} & 0 & 0 & 0 \end{bmatrix} = \begin{bmatrix} 0 & 0 & 0 & 0 & 590 & 0 \\ 0 & 0 & 0 & 590 & 0 & 0 \\ -191 & -191 & 430 & 0 & 0 & 0 \end{bmatrix} 10^{-12} C/N$$

Density 7750 kg/m^3

Figure 5.14. Material properties of piezoelectric actuators/sensors used in this study.

5.5 Transverse crack detection using Lamb wave

5.5.1 Embedded crack model

FEM models were developed for $[0_{16}]_T$ and $[0_6/90_4/0_6]_T$ orientated undamaged and damaged composite coupons with the crack in the middle four plies. A pictorial representation of the side view of damaged coupons for both orientations with the embedded crack and the corresponding Abaqus model with an attached PZT actuator before and after mesh generation is shown in Figure 5.15 and Figure 5.16. The area around the crack had a finer mesh to resolve the sudden variations in the stress/strain distribution.

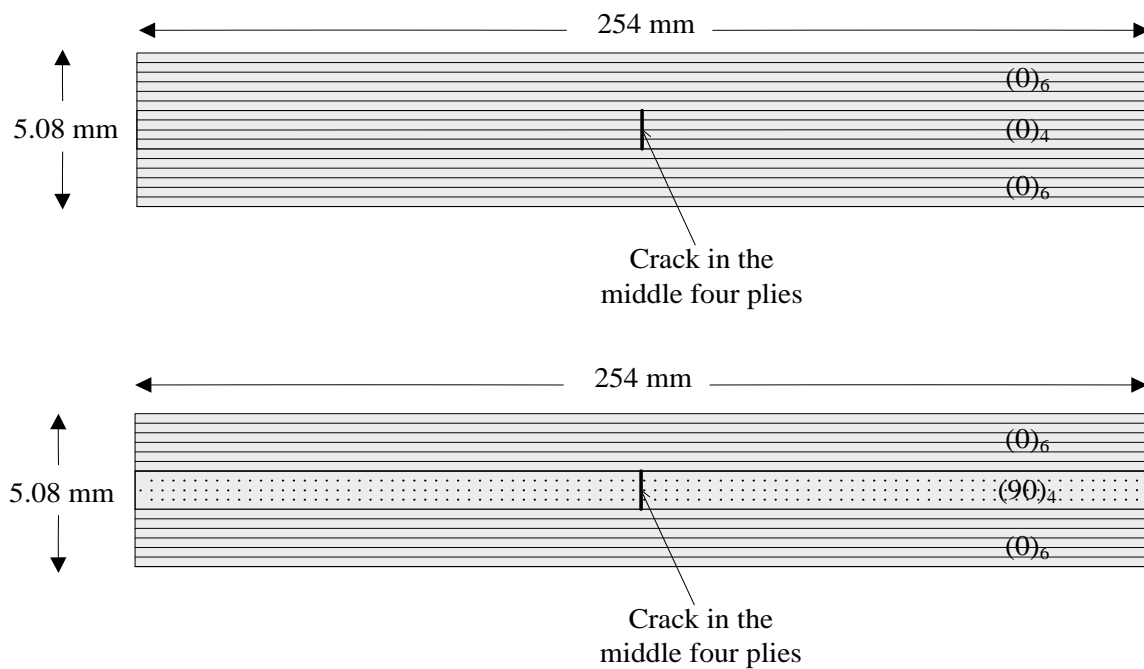


Figure 5.15. Pictorial representations of $[0_{16}]_T$ and $[0_6/90_4/0_6]_T$ composite coupons with an embedded crack in the middle four plies.

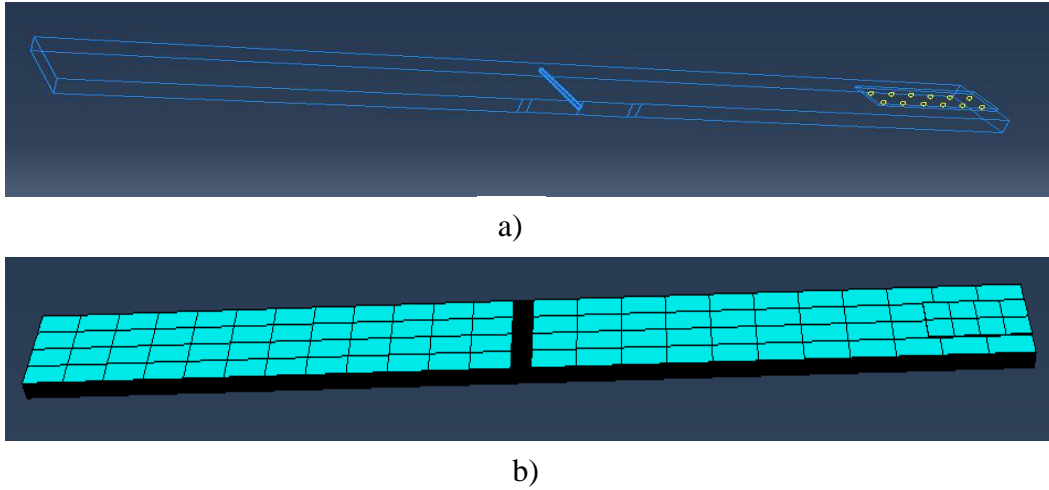


Figure 5.16. Abaqus models showing the embedded crack in a $[0_{16}]_T$ composite coupon: a) a wireframe model representation and b) a mesh representation.

A five cycle tone burst potential of center frequency 1 kHz was applied to the PZT actuator to generate lamb waves and the simulation was run for 10 ms. The lamb wave response for both undamaged and damaged composite coupons of $[0_{16}]_T$ and $[0_6/90_4/0_6]_T$ orientations are shown in Figure 5.17. The finite element results indicated less than 1% difference between an undamaged coupon and a coupon with an embedded crack. The damaged coupon response overlapped the undamaged coupon response showing no change in amplitude ratio or time of flight. The reflections from edges and cracks were found to be embedded in the transmitted signal due to low frequency actuation and the small distance between actuator and sensor. The simulation was repeated with a larger actuator, 38.1 mm \times 12.7 mm, to achieve higher deflection and the results for both orientations are shown in Figure 5.18. The results showed similar response as before although with larger reflections.

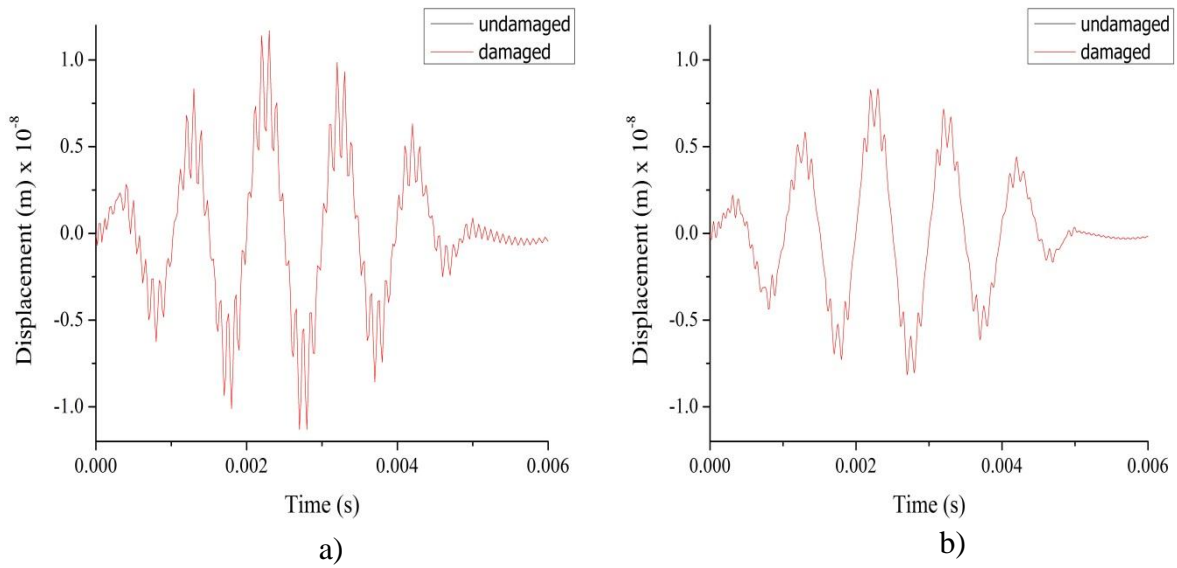


Figure 5.17. Finite element (FE) results comparing the lamb wave response of an undamaged coupon and a coupon with an embedded crack for: a) a $[0_{16}]_T$ composite coupon and b) a $[0_6/90_4/0_6]_T$ composite coupon.

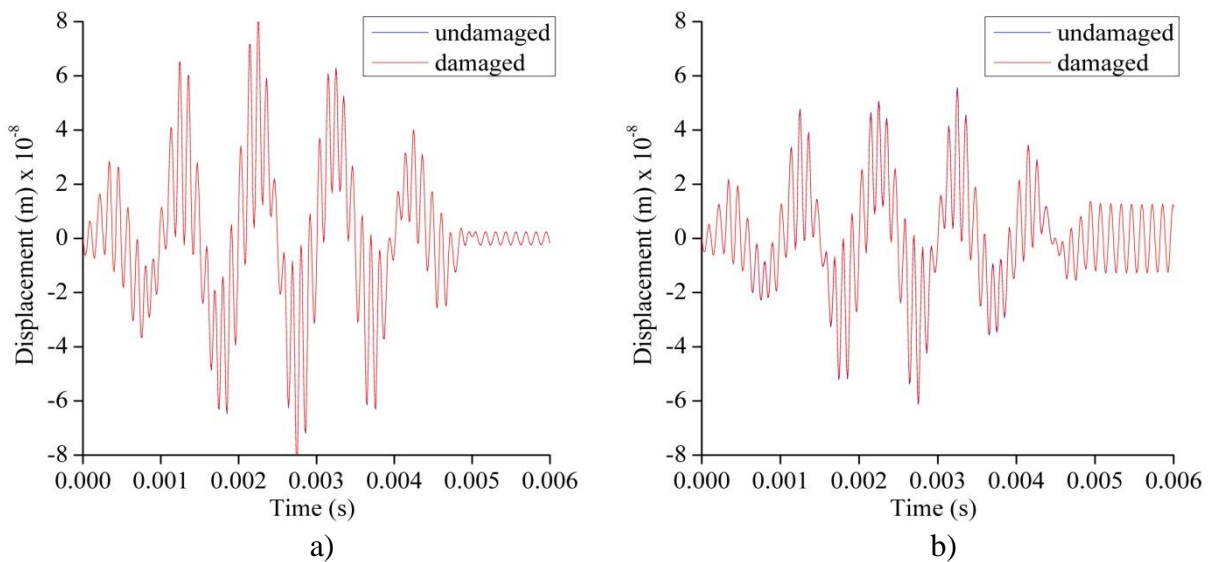


Figure 5.18. Finite element (FE) results comparing the lamb wave response of an undamaged coupon and a coupon with an embedded crack for: a) a $[0_{16}]_T$ composite coupon and b) a $[0_6/90_4/0_6]_T$ composite coupon for larger actuator.

5.5.2 Surface crack modeling

FEM models were developed for $[0_{16}]_T$ composite coupons with a surface crack of varying depth. The crack depth was reduced from four plies to one ply to study the relative difference in amplitude ratio between an undamaged composite coupon and a composite

coupon with a surface crack. A pictorial representation of side view of damaged coupons with surface crack of varying depth is shown in Figure 5.19.

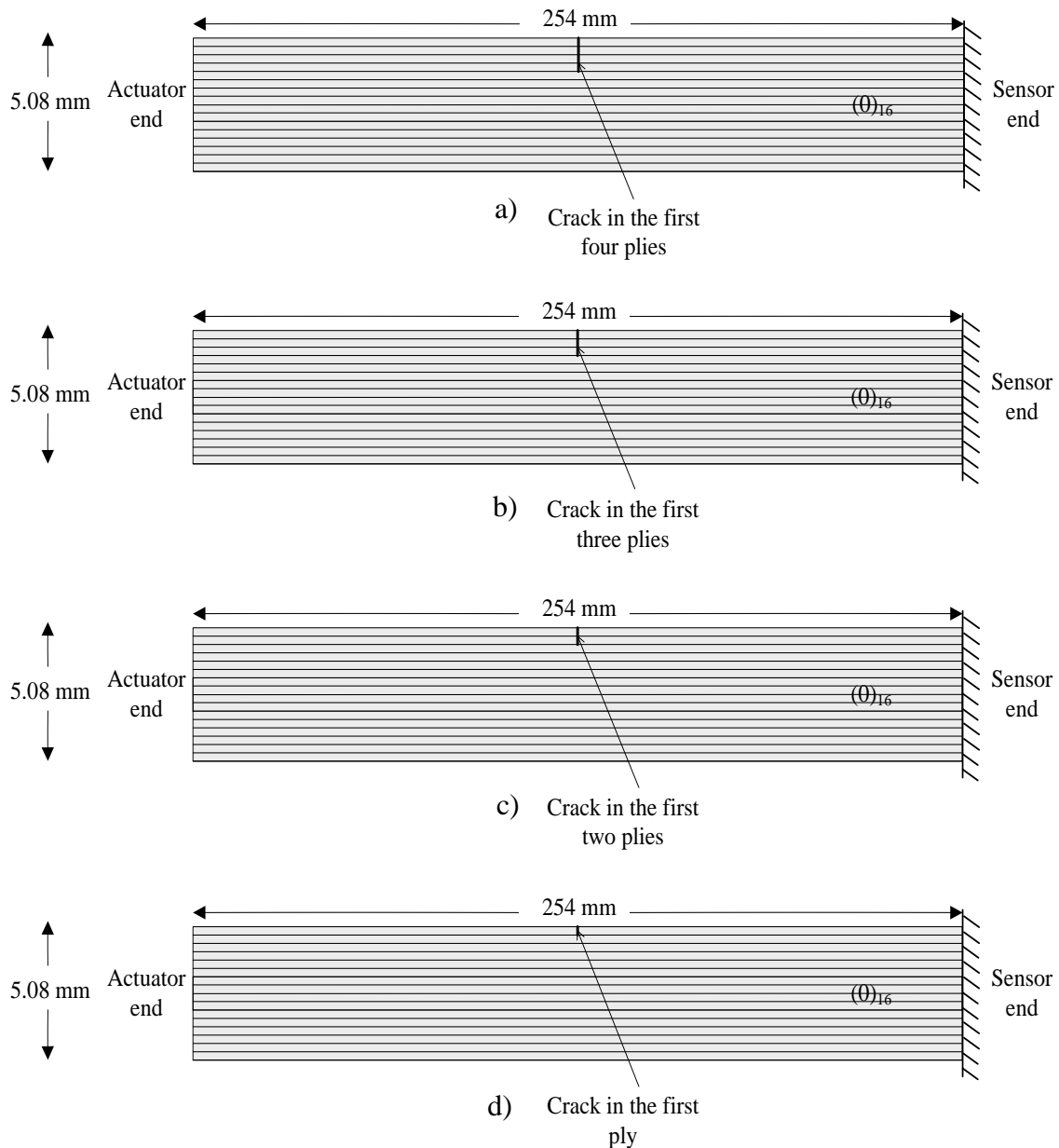


Figure 5.19. Pictorial representation of a $[0]_{16}$ composite coupon with surface cracks of varying depth: a) a surface crack in the first 4 plies; b) a surface crack in the first 3 plies; c) a surface crack in the first 2 plies; and d) a surface crack in the first ply only.

The results from these four cases (4, 3, 2 and 1 ply) are shown in Figure 5.20. A considerable change in amplitude ratio was observed for damaged coupons with a 4 ply deep surface crack and a 3 ply deep surface crack compared to an undamaged coupon. However, the change in amplitude ratio decreased for the 2 ply and 1 ply deep surface crack cases. The

reflections from edges and cracks were found to be embedded in the transmitted signal and no significant change in time of flight was observed due to low frequency actuation and the small distance between actuator and sensor.

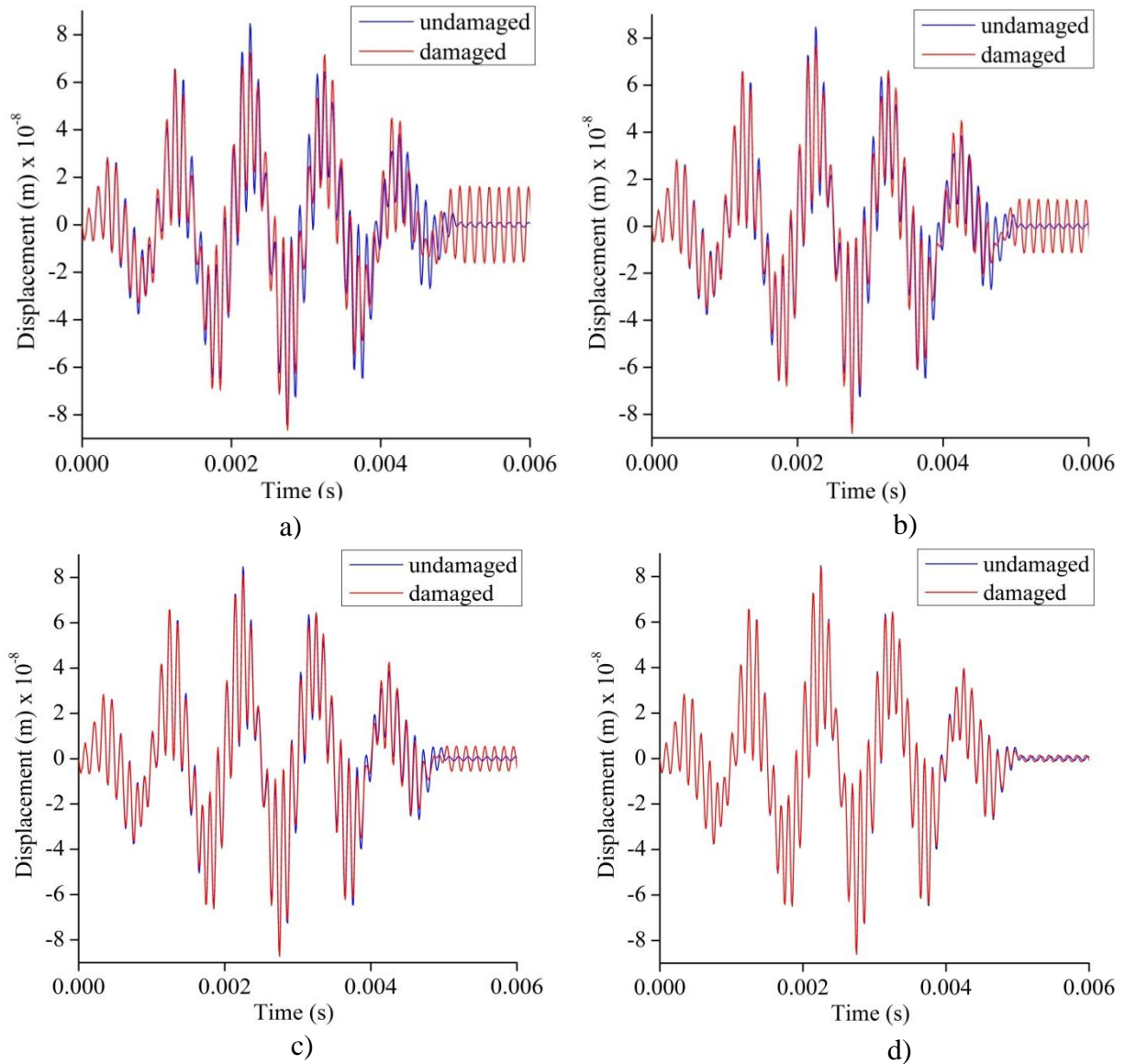


Figure 5.20. Finite element results comparing the lamb wave response of an undamaged $[0_{16}]_T$ composite coupon and a coupon with a surface crack for: a) a surface crack in the first 4 plies; b) a surface crack in the first 3 plies; c) a surface crack in the first 2 plies; and d) a surface crack in the first ply only.

5.5.3 Embedded crack at various depth

FEM models were developed for a $[0_{16}]_T$ composite coupon with a four ply deep embedded crack moved from the 2nd to 5th ply to the 7th to 10th ply as shown in Figure 5.21.

The crack was closer to the surface on which the actuator was placed.

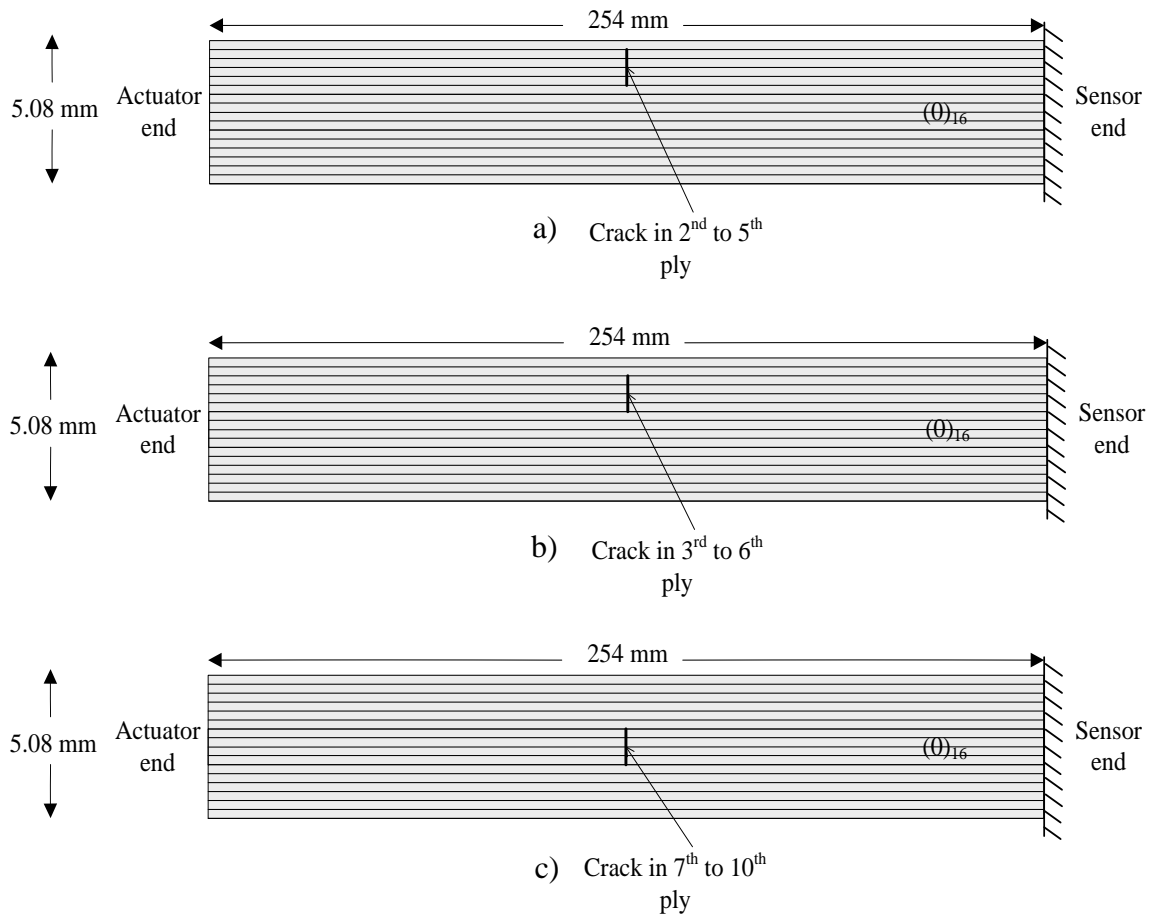


Figure 5.21. Pictorial representation of a $[0_{16}]_T$ composite coupon with a 4 ply deep embedded crack in: a) 2nd to 5th ply; b) 3rd to 6th ply; and c) 7th to 10th ply.

A sample result from the two cases, an embedded crack in ply 2 to ply 5 and an embedded crack in ply 3 to ply 6, is shown in Figure 5.22. The change in amplitude ratio reduced as the crack was moved deeper inside the coupon. The surface crack showed the maximum difference in amplitude between an undamaged and a damaged composite coupon, and the difference reduced to zero when the crack was located in the 4th ply to the 7th ply.

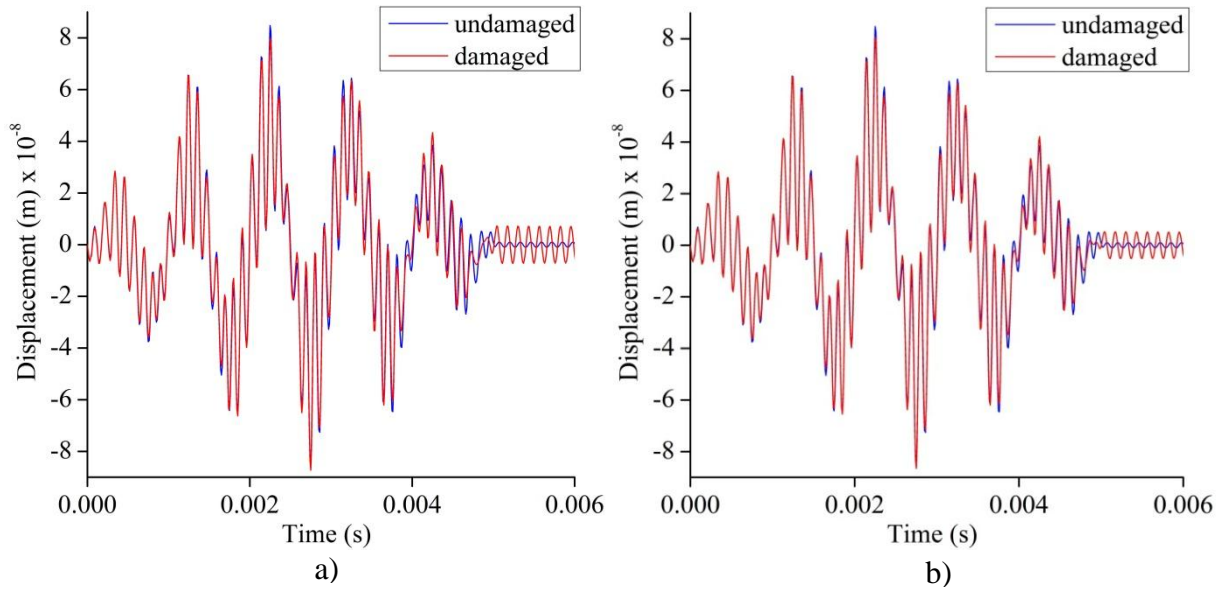


Figure 5.22. Finite element results comparing the Lamb wave response of a $[0_{16}]_T$ undamaged coupon and a coupon with a 4 ply deep embedded crack in: a) 2nd to 5th ply and b) 3rd to 6th ply.

5.5.4 A surface crack at various locations

FEM models were developed for a $[0_{16}]_T$ composite coupon with a four ply deep surface crack at various locations along the coupon. The composite coupon was clamped at one end with the PZT actuator surface-mounted on the opposite end. The Lamb wave response was obtained by reading the displacement data from the node 30 mm from the clamped end. The crack was moved from the actuator end to the fixed end as shown in Figure 5.23. Sample results for the crack near the actuator, the crack in the middle of the specimen and the crack near the fixed end is shown in Figure 5.24. The change in amplitude ratio reduced as the crack was moved away from the sensor/clamped end. The surface crack near the clamped end showed the maximum difference in amplitude ratio. However, large reflections from the edges were seen in the Lamb wave response. The results from these tests will be used in sensor placement optimization.

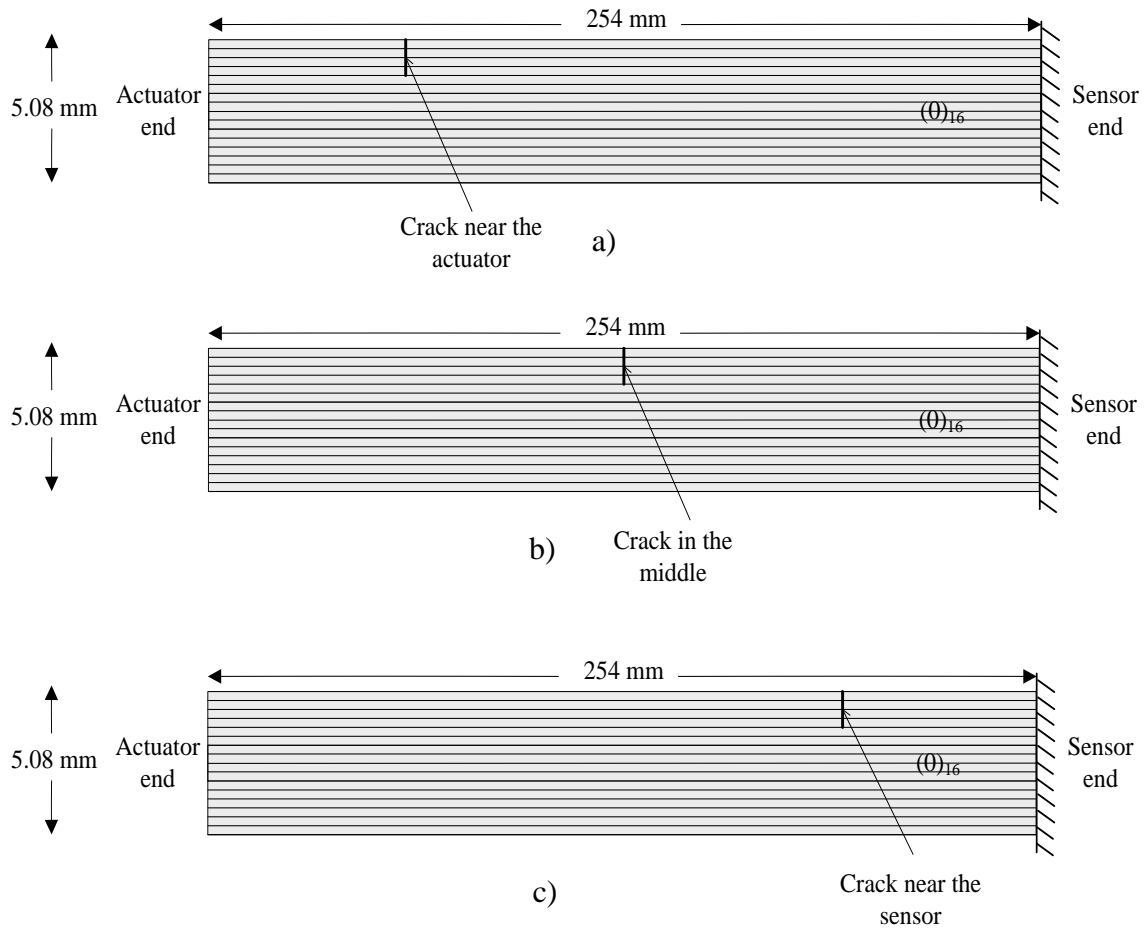


Figure 5.23. Pictorial representation of a $[0]_{16}_T$ composite coupon with a surface crack in the first four plies located: a) near the actuator end; b) in the middle; and c) near the sensor end.

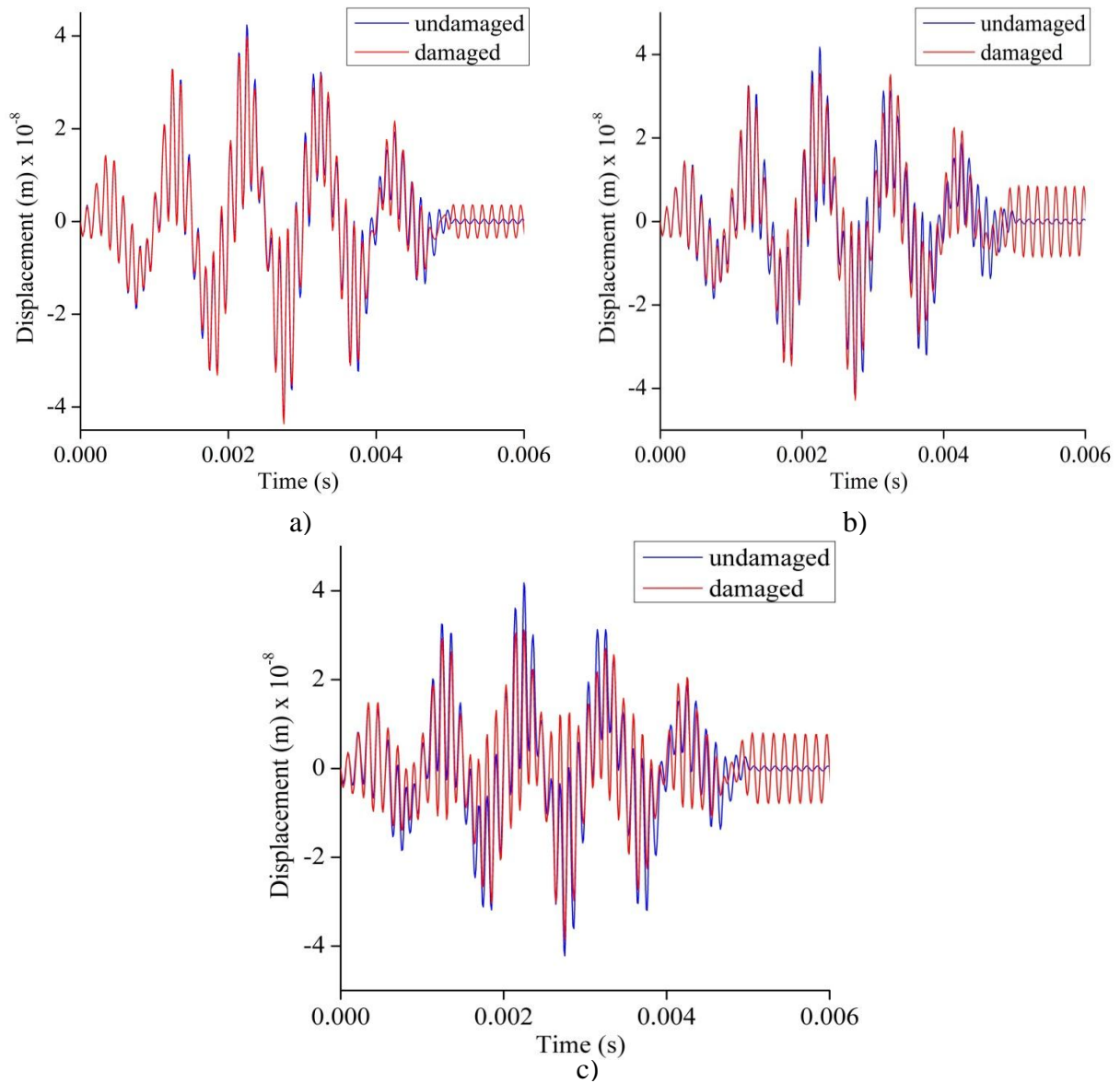


Figure 5.24. Finite element results comparing the Lamb wave response of a $[0_{16}]_T$ oriented undamaged coupon and a coupon with a surface crack in the first four plies located: a) near the actuator end; b) in the middle; and c) near the sensor end.

CHAPTER 6
RESULTS AND DISCUSSION

6.1 Comparison of experimental and modeling results

A comparison of experimental and modeling results was performed to study the accuracy of the results predicted by Abaqus. A reasonable confidence in modeling results enables one to expand the scope of testing to different configurations without physically performing the experiments. Reasonably close correlation was found between experimental and Abaqus modeling results. The results were matched for the experiment described in Chapter 4 comparing the Lamb wave response of an undamaged coupon to a coupon with a simulated crack in the first four plies. The composite coupon, supported on rollers at both ends of the specimen, was considered due to the possible errors in clamping torque when a clamped boundary condition is used. The displacement readings obtained from Abaqus were converted to an equivalent voltage by using Equation 6.1 [64, 65].

$$V_{\text{out}} = \frac{2Xt^2}{3L^2d_{31}} \quad (6.1)$$

where X is the displacement, t is the thickness of the piezoelectric actuator, L is the length of the beam, and d_{31} is the transverse piezoelectric coefficient.

Figure 6.1 shows less than 7% error between experimental and Abaqus results. The small differences observed can be attributed to the changes in the material properties due to minor fabrication differences from coupon to coupon and difference in the nature of bonding between the piezoelectric actuator and the coupon. The comparison results, after adjusting the longitudinal modulus are shown in Figure 6.2. The longitudinal modulus of the composite

coupon was decreased from 113 GPa to 105 GPa in the model to account for material variability.

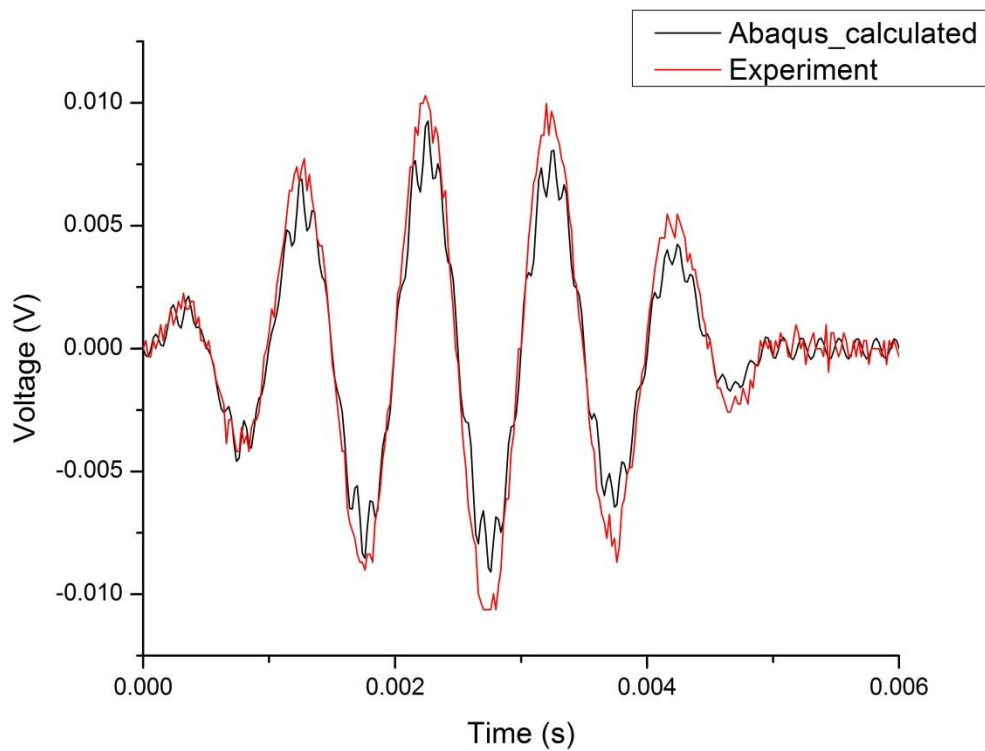


Figure 6.1. Comparison of experimental and Abaqus modeling results for an undamaged coupon.

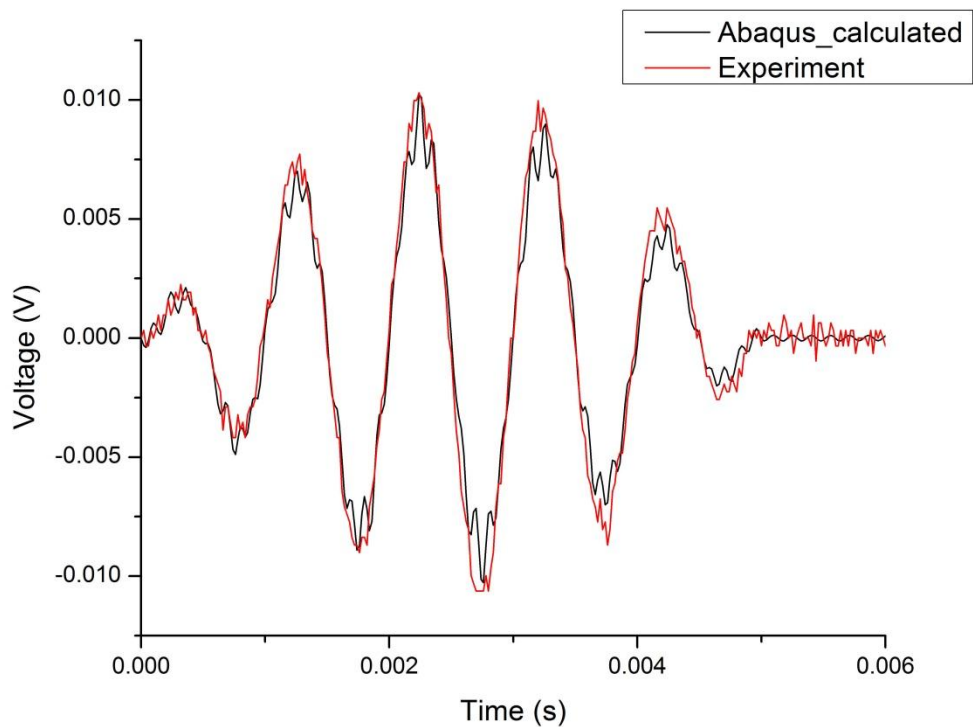


Figure 6.2. Comparison of experimental and Abaqus modeling results for an undamaged coupon after adjusting the modulus.

6.2 FFT analysis

A fast Fourier transform (FFT) analysis transforms a time domain function to a frequency domain function and was employed in our study to characterize the extent of damage for all cases. FFT efficiently separates the incident and reflected waves.

6.2.1 FFT analysis of an embedded crack

The comparison of frequency response of an undamaged composite coupon and a coupon with an embedded crack in the middle four plies for $[0_{16}]_T$ and $[0_6/90_4/0_6]_T$ orientations are shown in Figure 6.3, Figure 6.4, Figure 6.5 and Figure 6.6. It was observed that the incident signal at a frequency of 976.6 Hz and additional peaks at 7.617 kHz, 8.984 kHz and 11.4 kHz had almost the same amplitude for both undamaged and damaged cases. The enlarged views of the spectra show that the difference in amplitude is not significant in either orientation. The anti-symmetric mode Lamb waves (A_0) were found to be insensitive to the embedded crack for both $[0_{16}]_T$ and $[0_6/90_4/0_6]_T$ composite coupons. This observation indicates the importance of using the symmetric mode of Lamb waves (S_0) to detect damage through a certain thickness which is the case for an embedded crack [38, 54, 66].

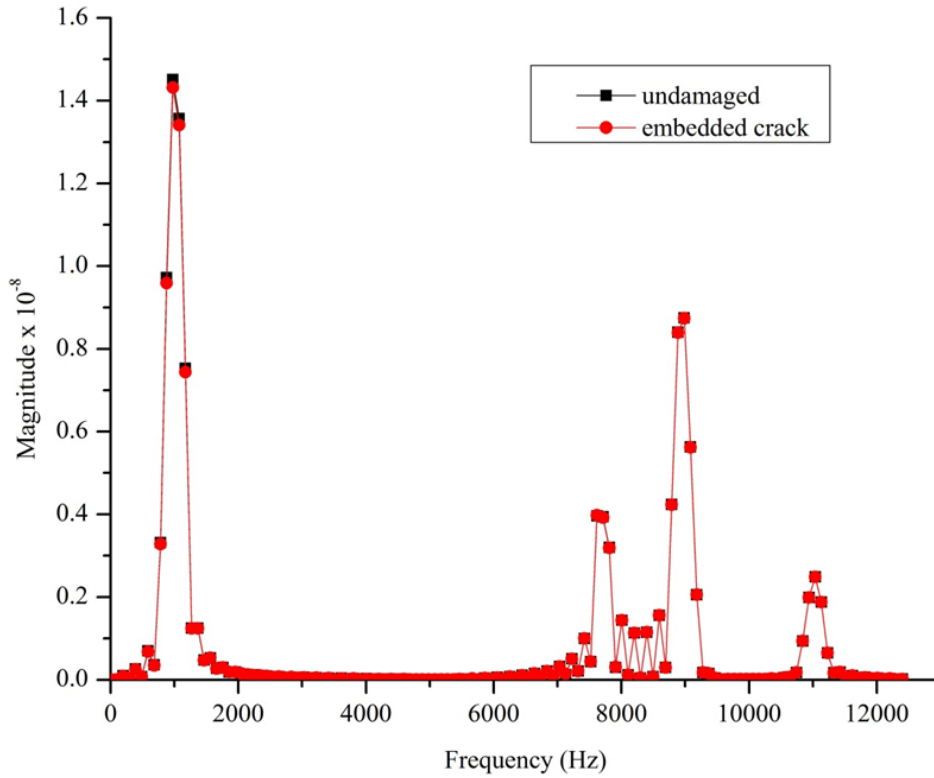


Figure 6.3. FFT spectrum based on Abaqus results comparing the frequency response of a $[0_{16}]_T$ orientation undamaged coupon and a coupon with an embedded crack in the middle four plies.

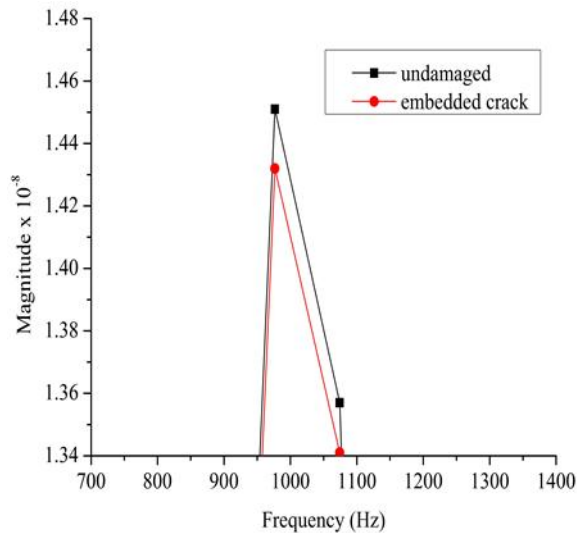


Figure 6.4. Enlarged view of a FFT spectrum at frequencies near 976.6 Hz showing less than 1% difference between the frequency response of a $[0_{16}]_T$ orientation undamaged coupon and a coupon with an embedded crack in the middle four plies.

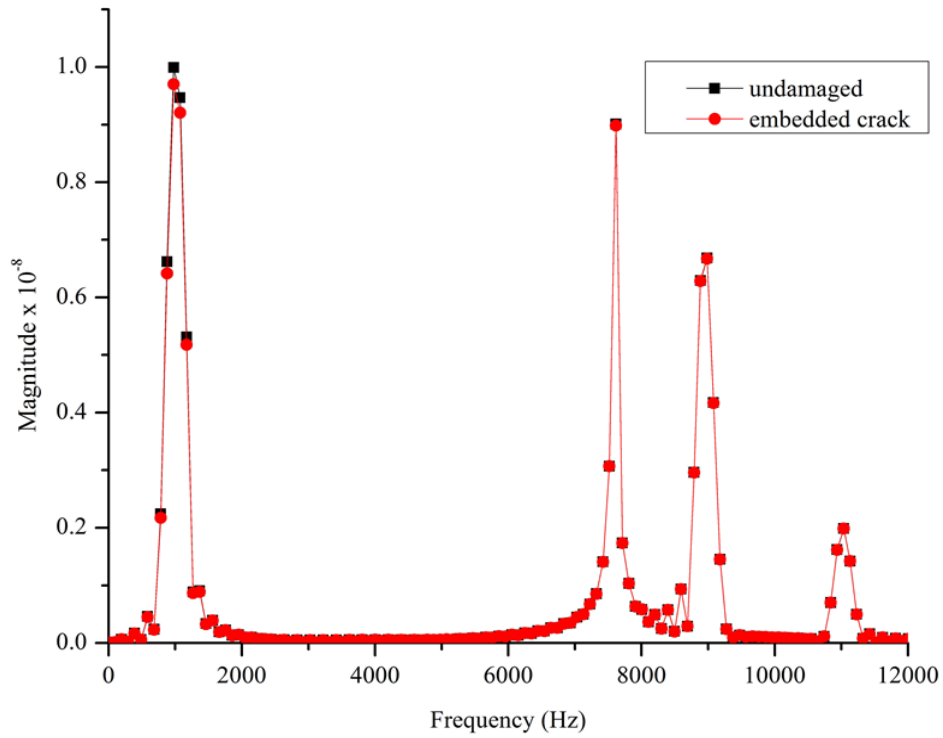


Figure 6.5. FFT spectrum based on Abaqus results comparing the frequency response of a $[0_6/90_4/0_6]_T$ orientation undamaged coupon and a coupon with an embedded crack in the middle four plies.

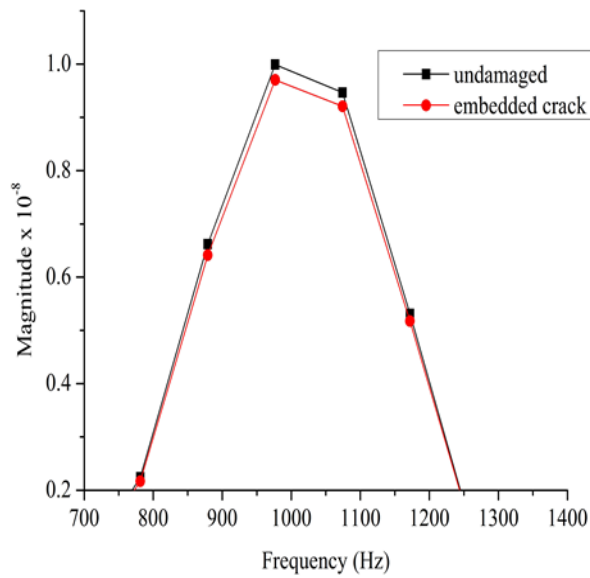


Figure 6.6. Enlarged view of a FFT spectrum at frequencies near 976.6 Hz showing less than 2% difference between the frequency response of a $[0_6/90_4/0_6]_T$ orientation undamaged coupon and a coupon with an embedded crack in the middle four plies.

6.2.2 FFT analysis of a surface crack

The FFT spectrum based on Abaqus results comparing the frequency response for an undamaged composite coupon and the coupons with a surface crack in varying numbers of plies is shown in Figure 6.7. The amplitude close to the input excitation frequency of 976 Hz was found to decrease with an increase in the level of damage. However, the amplitude at a frequency of 7.617 kHz was found to increase with an increase in the level of damage. This increase in amplitude with damage was attributed to the additional reflections from the crack and the degradation of the material stiffness. An enlarged view of the FFT spectrum at the two frequencies mentioned is shown in Figure 6.8. In addition, root mean square (RMS) deviation between an undamaged composite coupon and the coupons with a surface crack in varying number of plies is tabulated in Table 6.1 and shown in Figure 6.9. The coupon with a surface crack in four of its plies showed the maximum difference.

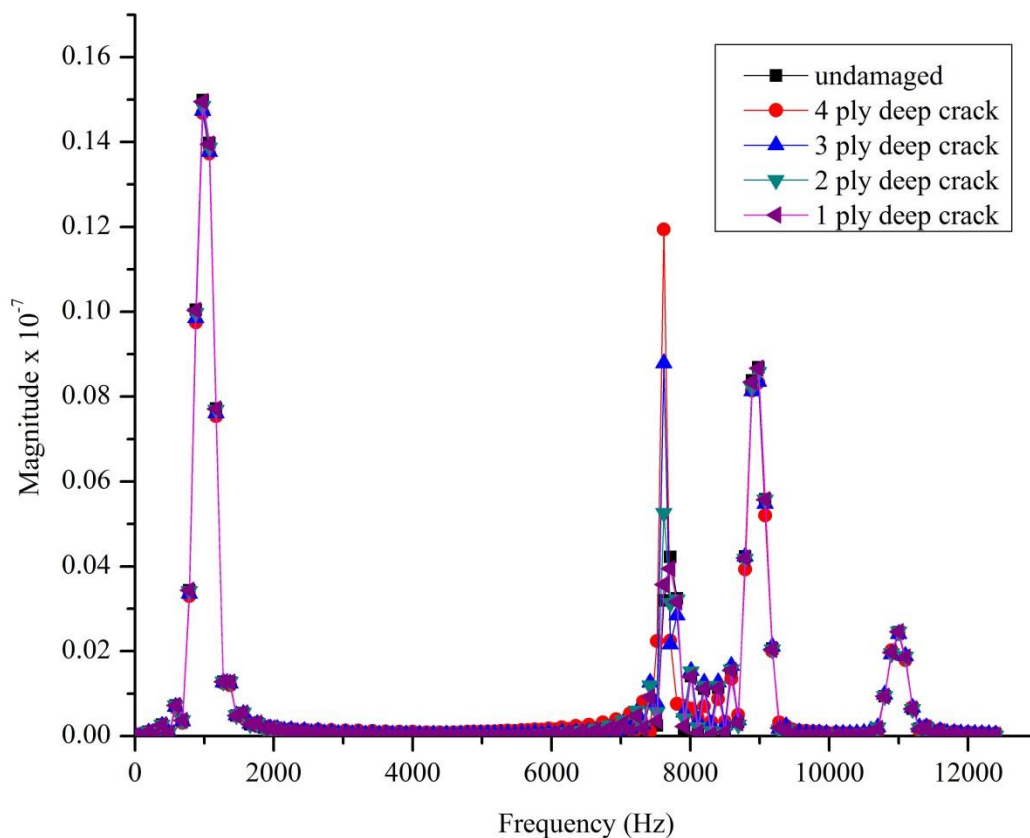


Figure 6.7. Complete FFT spectrum for $[0_{16}]_T$ composite coupons comparing the frequency response of undamaged to damaged coupons that is provided by varying the depth of a surface crack.

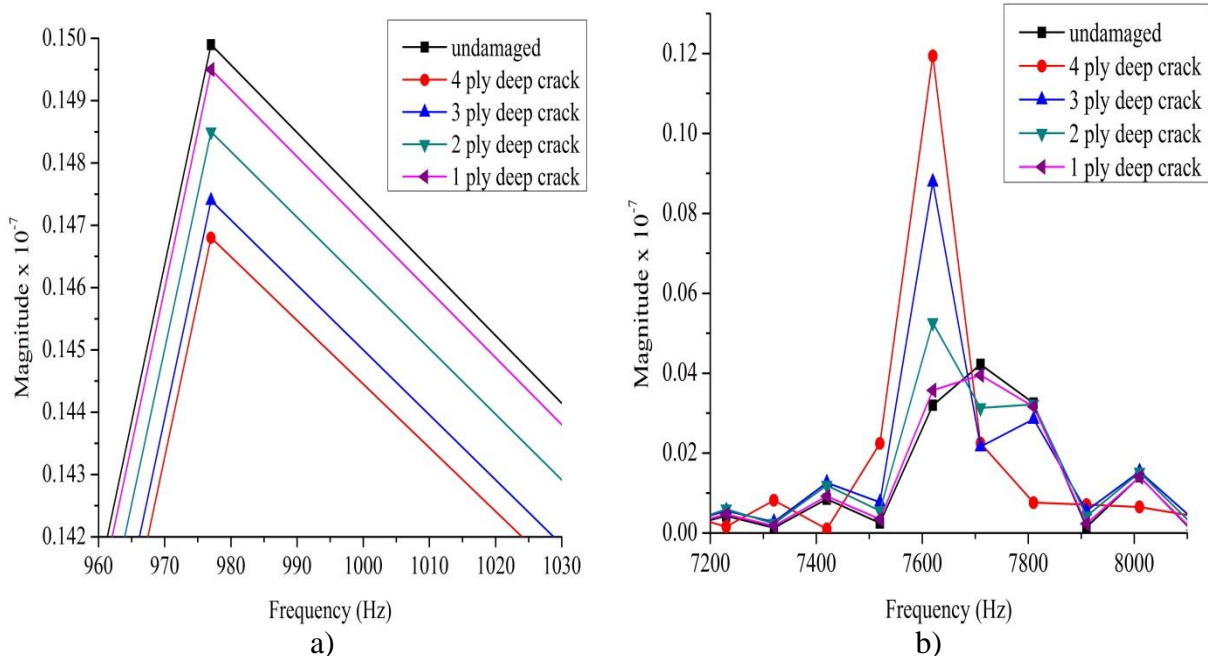


Figure 6.8. An enlarged view of FFT spectrum for an $[0_{16}]_T$ undamaged composite coupon and coupons with a surface crack of various depths for frequencies near: a) 976.6 Hz and b) 7.617 kHz.

Table 6.1. A table of RMS deviation between a $[0_{16}]_T$ undamaged coupon and coupons with a surface crack of various depths.

| Surface crack depth | RMS deviation between undamaged and damaged composite coupons (in m) |
|---------------------|--|
| 4 ply | 9.31509E-9 |
| 3 ply | 6.20763E-9 |
| 2 ply | 3.01265E-9 |
| 1 ply | 8.11465E-10 |

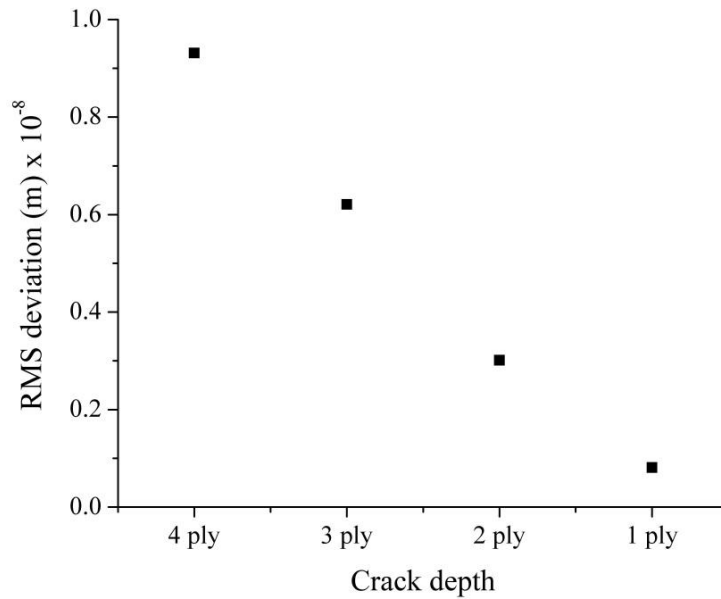


Figure 6.9. A graphical representation of RMS deviation between a $[0_{16}]_T$ undamaged coupon and coupons with a surface crack of various depths as a function of crack depth.

6.2.3 FFT analysis of a crack at various depths

The FFT spectra comparing the frequency response for an undamaged composite coupon and coupons with a four ply deep crack at various depths are shown in Figure 6.10. The amplitude close to the input excitation frequency of 976 Hz was found to increase as the crack was moved deeper inside the specimen. However, the amplitude at a frequency of 7.617 kHz was found to be highest for the surface crack and reduced considerably as the crack was moved deeper inside the specimen. An enlarged view of the FFT spectrum at the two frequencies mentioned is shown in Figure 6.11. In addition to FFT analysis, RMS deviation between an undamaged coupon and coupons with a four ply deep crack at various depths was calculated and is tabulated in Table 6.2 and shown in Figure 6.12. The difference between an undamaged coupon and a damaged coupon decreased exponentially once the crack location was moved inside the coupon.

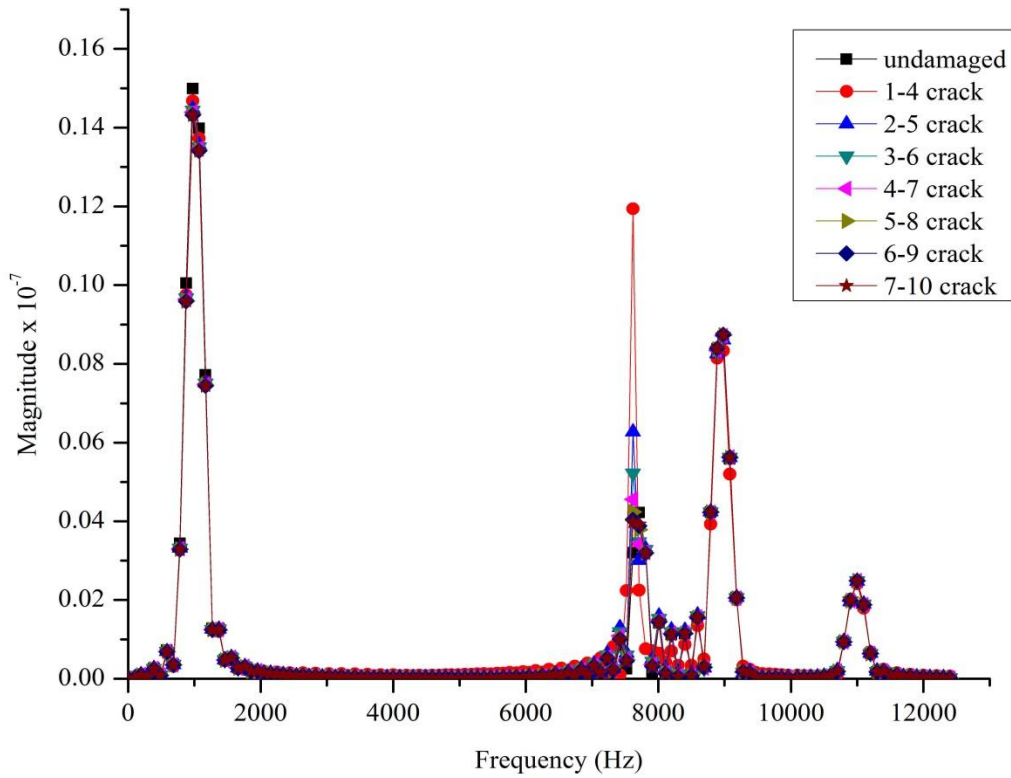


Figure 6.10. Complete FFT spectrum for $[0_{16}]_T$ composite coupons comparing the frequency response of an undamaged coupon to coupons with a four ply deep crack at various depths.

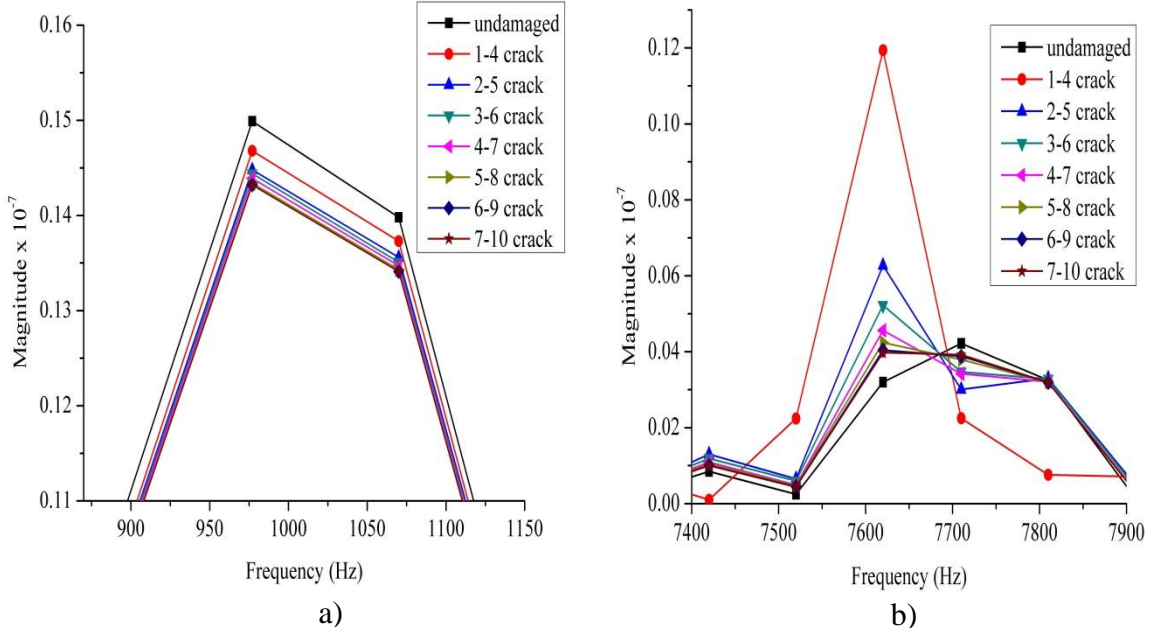


Figure 6.11. An enlarged view of a FFT spectrum for an $[0_{16}]_T$ undamaged composite coupon and coupons with a four ply deep surface crack at various depths at frequencies near: a) 976.6 Hz and b) 7.617 kHz.

Table 6.2. A table of RMS deviation between a $[0_{16}]_T$ undamaged composite coupon and coupons with a four ply deep crack at various depths along the coupon.

| Crack location (Ply numbers) | RMS deviation between undamaged and damaged composite coupons (in m) |
|------------------------------|--|
| 1 - 4 | 9.31509E-9 |
| 2 - 5 | 3.93624E-9 |
| 3 - 6 | 2.90688E-9 |
| 4 - 7 | 2.30248E-9 |
| 5 - 8 | 1.89218E-9 |
| 6 - 9 | 1.66387E-9 |
| 7 - 10 | 1.58609E-9 |

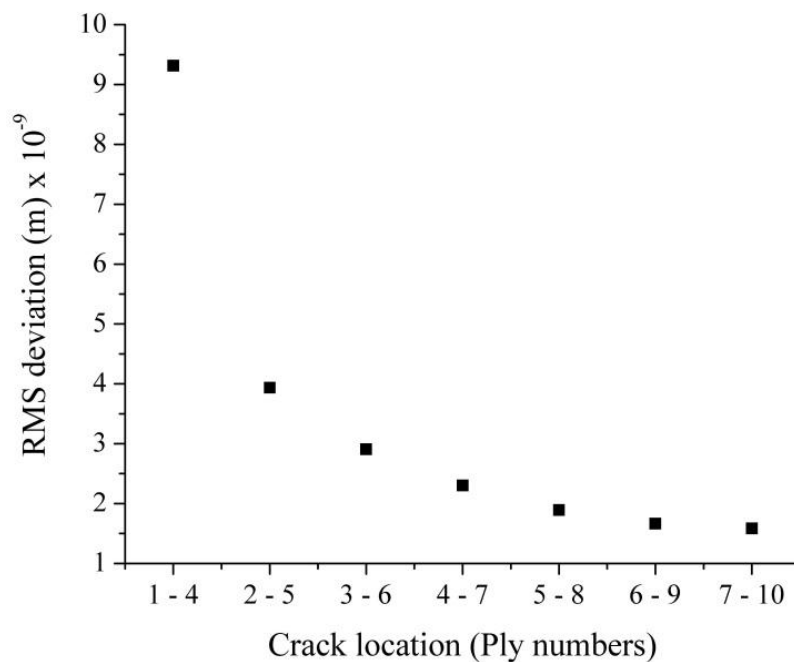


Figure 6.12. A graphical representation of RMS deviation between a $[0_{16}]_T$ undamaged composite coupon and coupons with a four ply deep crack at various depths as a function of crack location.

6.2.4 FFT analysis of a surface crack at various locations

The FFT spectra comparing the frequency response for an undamaged composite coupon and the coupons with a four ply deep surface crack at various locations across the coupon are shown in Figure 6.13. The amplitude at a frequency of 976.6 Hz was highest for the undamaged coupon and reduced as the crack moved towards the clamped end. However, the amplitude at a frequency of 7.617 kHz was found to be highest for a surface crack near the clamped end and reduced considerably as the crack was moved away from the sensor. An

enlarged view of the FFT spectrum at the two frequencies mentioned is shown in Figure 6.14. In addition to FFT analysis, RMS deviation between an undamaged coupon and coupons with a four ply deep crack at various locations across the coupon was calculated and is tabulated in Table 6.3 and shown in Figure 6.15. The difference between an undamaged coupon and a damaged coupon was maximum when the crack location was close to the sensor.

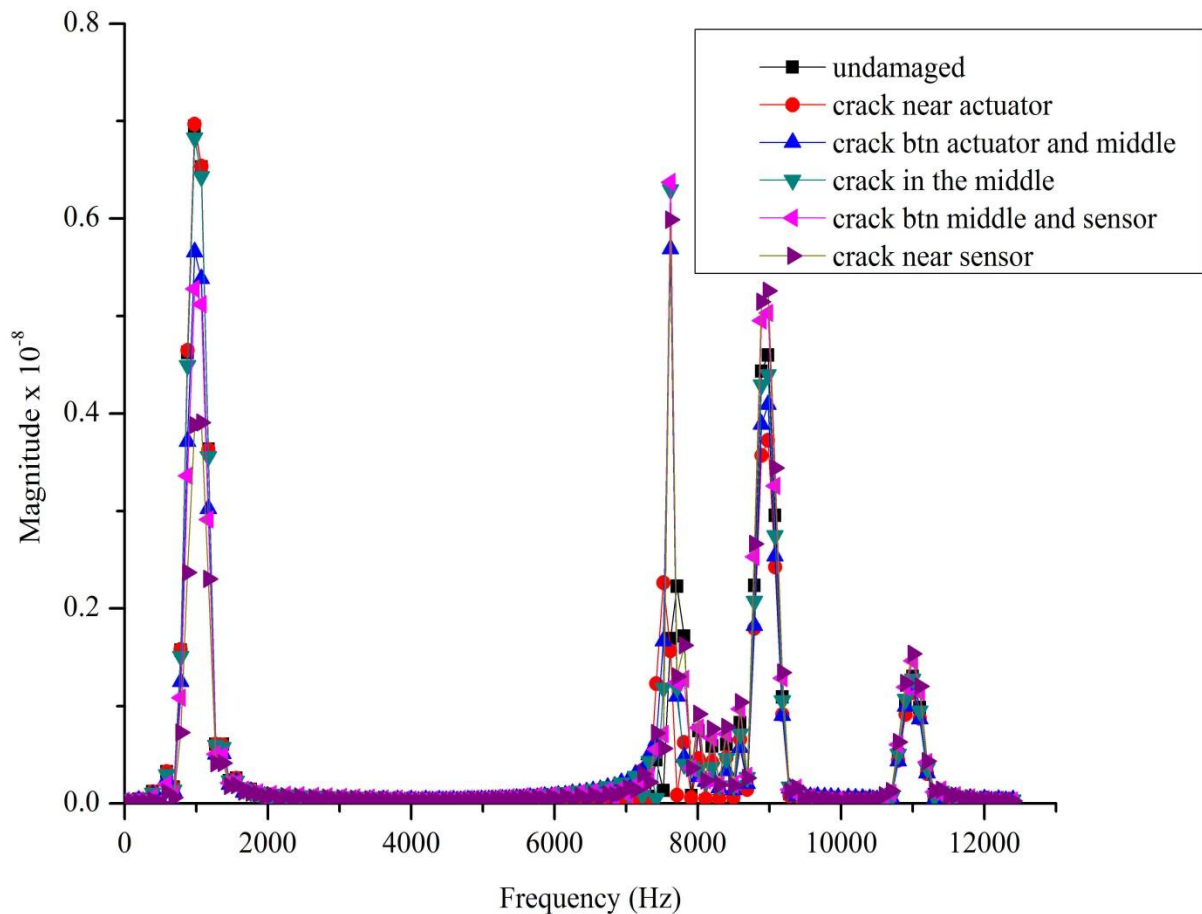


Figure 6.13. Complete FFT spectrum for $[0_{16}]_T$ composite coupons comparing the frequency response of undamaged coupon to coupons with a four ply deep surface crack at various locations across the coupon.

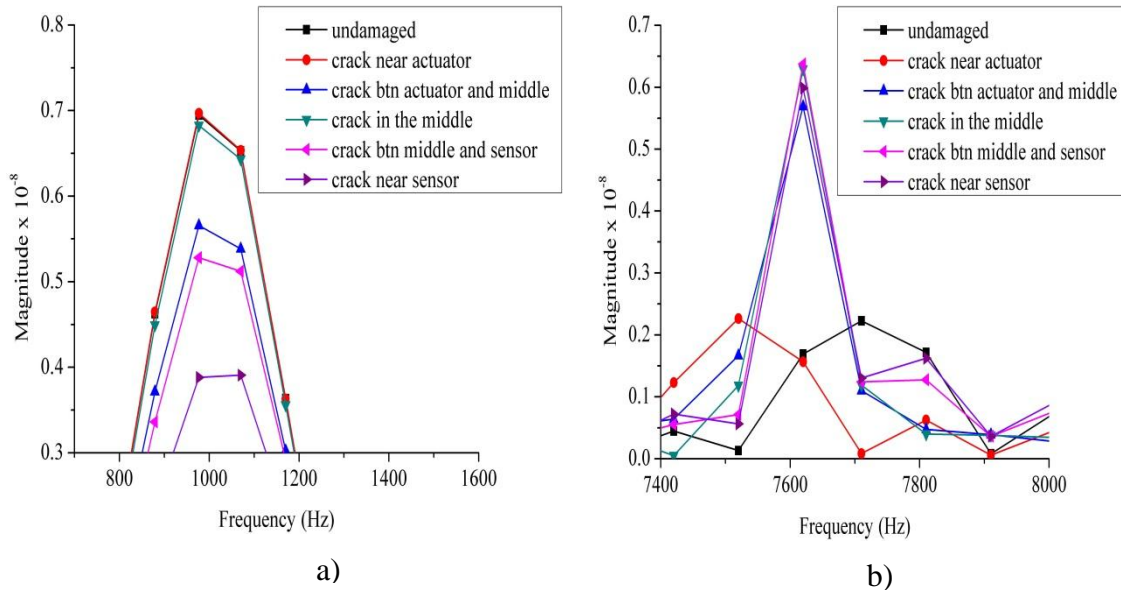


Figure 6.14. Enlarged view of FFT spectrum for an $[0_{16}]_T$ undamaged composite coupon and coupons with a four ply deep surface crack at various locations at frequencies near: a) 976.6 Hz and b) 7.617 kHz.

Table 6.3. A table of RMS deviation between a $[0_{16}]_T$ undamaged composite coupon and coupons with a four ply deep surface crack at various locations across the coupon.

| Distance of crack location from actuator end (cm) | RMS deviation between undamaged and damaged composite coupons (in m) |
|---|--|
| 5 | 3.50717E-9 |
| 7.5 | 4.79919E-9 |
| 12.5 | 4.91053E-9 |
| 17.5 | 4.98842E-9 |
| 20 | 5.50103E-9 |

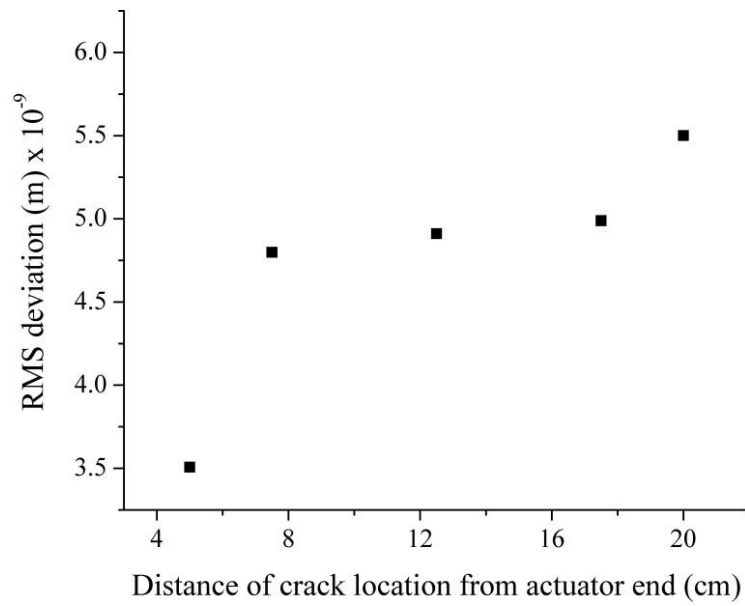


Figure 6.15. A graphical representation of RMS deviation between an $[0_{16}]_T$ undamaged composite coupon and coupons with a four ply deep surface crack at various locations across the coupon.

The results from all of the tests conducted in this research give an estimate of the sensor sensitivity and sensor coverage. This information can be used as inputs to optimize the placement of sensors and develop an ideal damage detection system.

CHAPTER 7

FINITE ELEMENT MODEL FOR OPTIMIZATION

7.1 Interface between MATLAB and Abaqus

Optimal sensor placement and sensor density is critical for reliable damage detection. A large number of sensors increases the damage detection capability but increases the power, cost and weight. Different approaches such as genetic and evolutionary algorithms [54] and stable noisy optimization by branch and fit (SNOBFIT) [55] have been used to achieve sensor placement optimization (SPO). Guratzsch *et al.* [67] proposed a four step method for sensor placement optimization. They performed the finite element analysis by modeling the plate thickness and material properties (Young's modulus, Poisson's ratio and density) as a Gaussian random field. Each node of the finite element model was considered for a probable sensor location and the SNOBFIT algorithm was used for SPO.

A similar approach was followed by our group to achieve SPO. Finite element models for undamaged and damaged specimens were developed using Abaqus. MATLAB was used to call Abaqus in a loop to achieve the desired number of data sets for a particular damage case study. Each Abaqus run was called after regenerating the input file with a new value for a material property within the experimentally determined standard deviation. A suitable feature set (strain, displacement, and natural frequency) was written to the report files. The data was recorded only for the top surface nodes as the goal was to optimize sensor placement on the top surface of the specimen only. Embedding the sensors or placing sensors on the sides or bottom of the coupon were not considered in this research project. The process flow is presented in Figure 7.1.

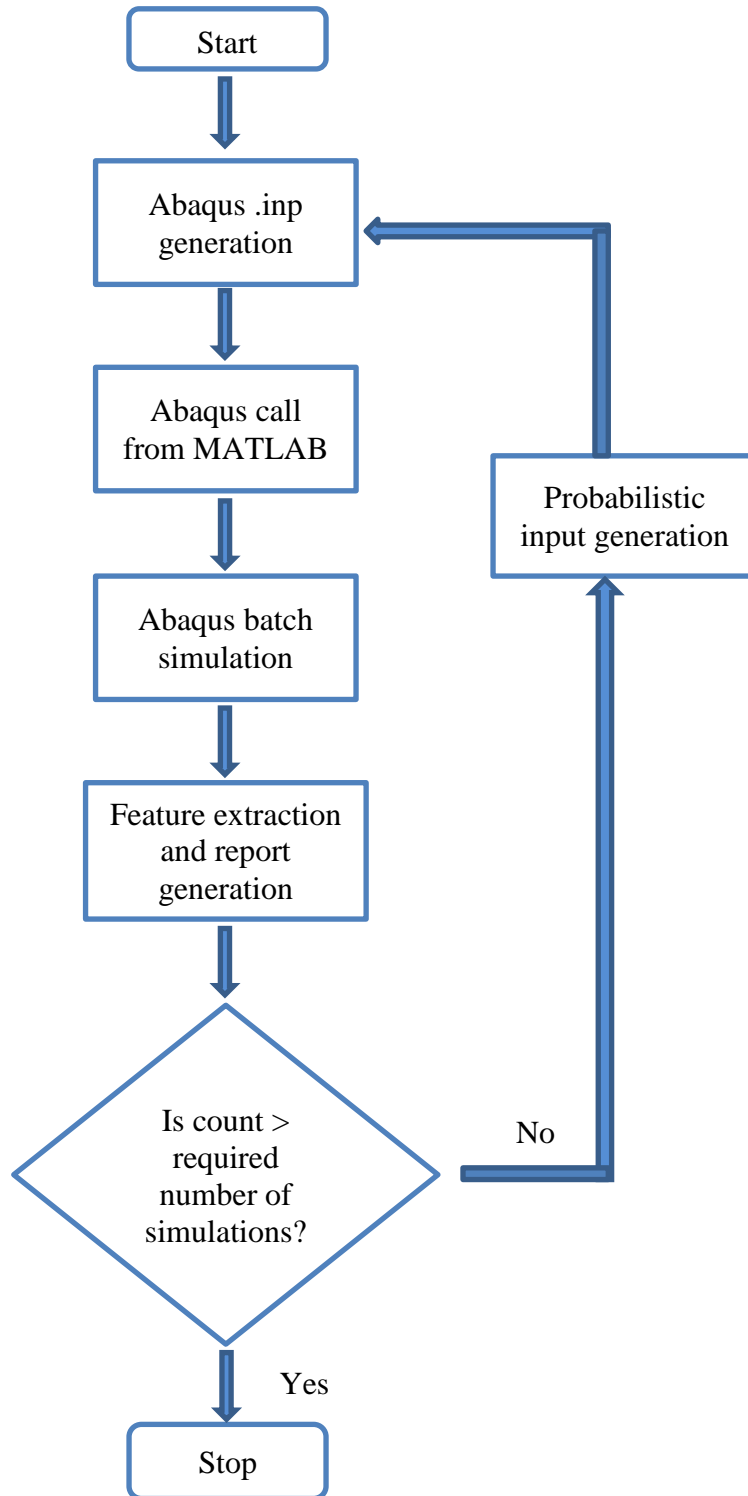


Figure 7.1. A flow chart demonstrating the interface between MATLAB and Abaqus that used for generating data set for sensor placement optimization (where count is the iteration number).

7.2 Embedded crack test

The composite coupon used for the embedded crack test had dimensions of 304.8 mm \times 25.4 mm \times 3.175 mm, with ply orientation $[0_{16}]_T$ and the geometry was discretized using 19200 linear hexahedral elements of type C3D8R. Damage was introduced by assigning a crack for the middle four plies at the center of the coupon. The coupon was supported on rollers at one end and was subjected to an axial tensile load at the opposite end. For this test 90 simulations were run, 45 simulations of the undamaged model and 45 simulations with a crack in the middle four plies with varying material properties. The longitudinal strain contour plot for the damaged case is shown in Figure 7.2. The static strain values measured from 30 undamaged simulation cases at all of the surface nodes was used to train the classifier.

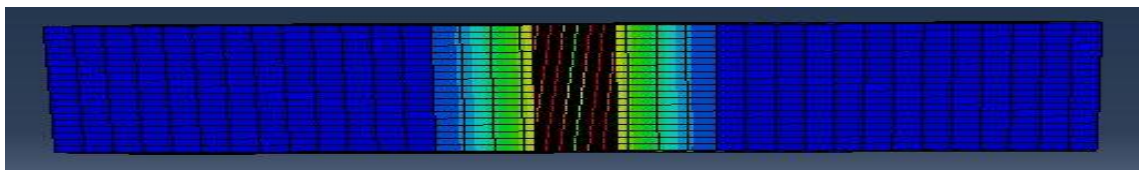


Figure 7.2. A FE representation of longitudinal strain component contour plot observed on the top surface of a composite coupon with an embedded crack in the middle.

The aim of the experiment was to find the optimal sensor placement given the damage at a specific location. The process flow is summarized in Figure 7.3.

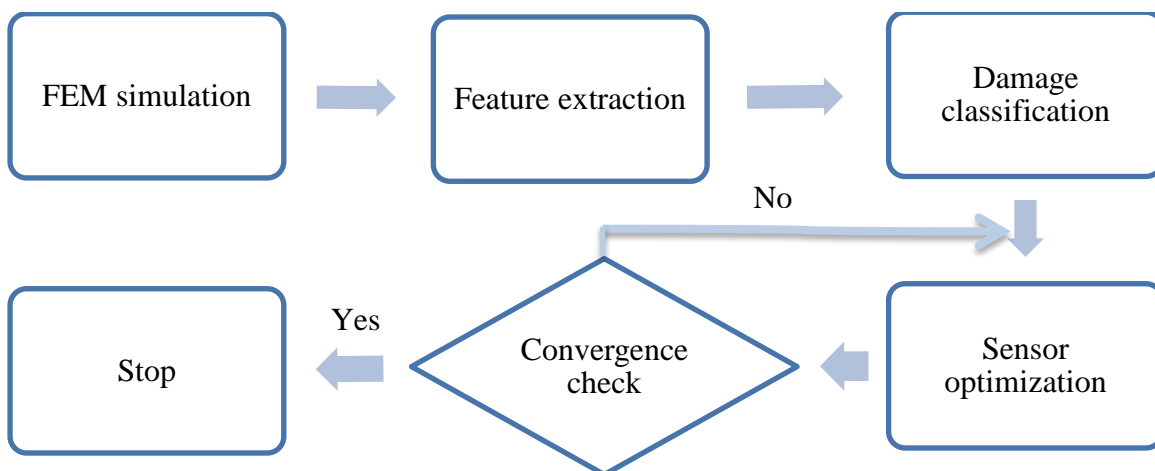


Figure 7.3. A flow chart demonstrating the sensor placement optimization process.

Damage classification was performed using both artificial neural network (ANN) and support vector machines (SVMs). Sensor optimization was performed using the evolutionary strategy. A sample result has been added in this section for illustration. This result came from the work led by Muhammad Farooq [68]. Figure 7.4 shows the initial random placement of sensors at the beginning of the algorithm. Figure 7.5 shows the final placement of sensors proposed by the optimization algorithm. It was observed that the sensors moved towards the damaged region, as expected.

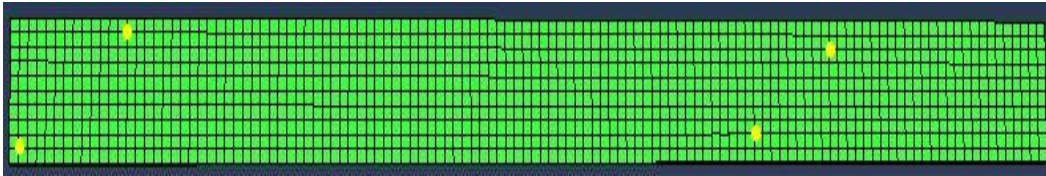


Figure 7.4. Random placement of sensors at the beginning of optimization algorithm (dots represent sensors).

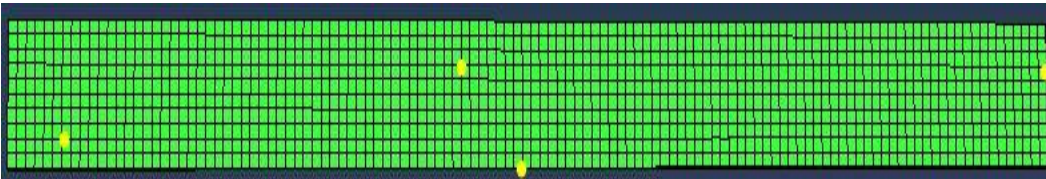


Figure 7.5. Final placement of sensors after the completion of optimization algorithm (dots represent sensors).

A similar approach could be extended to optimize the sensor placement for dynamic simulation and different damage cases as well as damage at different locations.

CHAPTER 8

CONCLUSIONS AND FUTURE WORK

8.1 Conclusions

A reliable structural health monitoring system offers enormous improvements in safety in addition to economic benefits by performing maintenance based on the condition of a structure rather than maintenance based on an estimated time. Given these advantages, it is important to have a suitable damage detection system especially for large, expensive structures. In this thesis, numerical modeling was combined with an experimental study using a Lamb wave-based approach to detect a transverse crack in a composite coupon. Undamaged coupons and coupons with damage in the form of both embedded and surface cracks were fabricated using a VARTM process. Surface mounted PZT actuators and PZT sensors were used for actuation of Lamb waves in the composite materials and in sensing the response of the structure. The actuation parameters and the choice of transducers were made based on a review of the literature. National Instruments LabVIEW software was used to synchronize the actuation initiation and response measurement. Transverse surface crack detection using a surface mounted PZT actuator and a surface mounted PZT sensor was experimentally demonstrated.

The experimental study was supported by finite element models developed using Abaqus, a commercial finite element software. A good correlation was observed between the experimental and finite element modeling results. Eight node linear brick elements and eight node piezoelectric elements were used to model the composite coupon and PZT actuator, respectively. The element type and mesh resolution were finalized after conducting a set of benchmarking tests. Finite element modeling results from both crack modeling benchmark

and dynamic simulation benchmark tests confirmed the accuracy of the models developed using Abaqus. Finite element models were used to expand the scope of testing from four ply deep surface cracks to transverse cracks of various depths and transverse cracks at various locations. Finite element models were also used to generate a simulation data set for sensor placement optimization.

The results from experimental and numerical modeling studies showed that A_0 mode Lamb waves carried sufficient information to detect a surface crack in a composite coupon. A fast Fourier transform analysis was performed to characterize the damage. The amplitude value of the Lamb waves was found to increase with an increase in crack depth. It was also found that it was easier to classify the damage when the crack was located near the sensor. However, the A_0 mode Lamb waves were insensitive to an embedded transverse crack in a composite coupon. The sensitivity of Lamb waves decreased as the crack was moved from the top four plies to the middle four plies of a 16 ply composite coupon. Both experimental investigation and finite element models indicated poor detection of embedded cracks using A_0 mode Lamb waves.

A detailed description of a damage detection system, results from finite element models, and a review of the limitations and capabilities of anti-symmetric mode Lamb waves in transverse crack detection were discussed in this thesis. This information can be utilized in developing a reliable structural health monitoring system.

8.2 Recommendations for future work

The actuation frequency plays a very important role in generating the desired mode Lamb waves and also in deciding the level of damage that can be detected. The wavelength of actuation frequency should be on the order of, or comparable to, the damage length to efficiently classify the damage. Thus a high frequency of actuation helps in detecting smaller size of damage. However, a higher frequency will generate multiple modes and also

deteriorate the signal to noise ratio. A careful selection of frequency is required for these reasons. An additional improvement would be to embed the sensors during fabrication of composite panels and study the Lamb wave response for transducers as a function of temperature. A different actuator/sensor type such as the MFC patch or FBG sensors may show improved performance for certain applications.

A_0 mode Lamb waves were found to be insensitive to embedded cracks and there are suggestions in the literature that S_0 mode Lamb waves are a better choice in such a case. The existing damage detection setup could be modified to generate symmetric mode Lamb waves by using two co-located actuators. This would require an additional amplifier and a two channel waveform generator.

This thesis focused primarily on detecting transverse crack damage. Delamination, another type of damage, can also be a predominant source of damage in composite materials. A similar fabrication procedure and SHM system setup can be used to detect delamination in composite materials in the future.

Finite element models should be investigated more to model the real time noise and surface irregularities in the composite coupons. The model could be modified to replicate the damping in the structure and the residual stresses inherent in the composite coupons.

This thesis presented a case study showing the result of sensor placement optimization for a composite coupon with an embedded crack. However, the tests considered static strain values as the feature vector set. The existing setup can be extended to perform dynamic analysis tests and extract frequency domain as well as time domain features for damage classification and sensor placement optimization.

REFERENCES

- [1] J. Teresko, "Boeing 787: A Matter of Materials -- Special Report: Anatomy of a Supply Chain," *Industry Week*, 2007.
- [2] Gerald and Dillingham, "Status of FAA's Actions to Oversee the Safety of Composite Airplanes," 2011.
- [3] M. O. W. Richardson and M. J. Wisheart, "Review of low-velocity impact properties of composite materials," *Composites Part A: Applied Science and Manufacturing*, vol. 27, pp. 1123-1131, 1996.
- [4] NTSB, "Aviation Accident Report," Washington, USA1989.
- [5] NASA, "Columbia Accident Investigation Board Report," Washington, USA2003.
- [6] NTSB, "Photo of Boeing 737-297 N73711," ed, 1988, pp. Kahului Airport, HI
- [7] D. Agnos, "CBS, Tom Coburn, Dow Constantine Wag Fingers at Our Stimulus Spending," *Seattle Weekly*, 2009.
- [8] K. Majcher, "10 Technologies To Watch," 2011.
- [9] R. Waugh, "Not just a load of hot air: Dream becomes reality as Boeing's new carbon-fibre 787 Dreamliner heralds a new age of air travel," 2011.
- [10] R. R. Ramlogun, B. Picoux, L. Ulmet, and C. Petit, "An evaluation of the application of infrared thermography in the diagnosis of civil engineering structures," in *10th International Conference on Civil, Structural and Environmental Engineering Computing, Civil-Comp 2005, August 30, 2005 - September 2, 2005*, Rome, Italy, 2005.
- [11] F. Chen, L. Guo, L. Xiao, and L. Liu, "The principle and application of the laser ultrasound non-destructive testing technology," in *2010 International Conference on Display and Photonics, July 12, 2010 - July 13, 2010*, Nanjing, China, 2010, p. International Computer Science Society; Central China Normal University; Intelligent Inf. Technol. Appl. Res. Assoc.
- [12] R. Gregory, "Laser shearography inspection for aircraft and space structures," *Insight: Non-Destructive Testing and Condition Monitoring*, vol. 43, pp. 150-154, 2001.
- [13] J. Zhang, Y. Liu, and Y. Chen, "X-ray radiography used for non-destructive testing on welds of steel bridge," in *Progress in Safety Science and Technology, October 10, 2002 - October 13, 2002*, Taian, China, 2002, pp. 419-423.

- [14] H. Sohn, C. R. Farrar, F. M. Hemez, and J. J. Czarnecki, *A Review of Structural Health Review of Structural Health Monitoring Literature 1996-2001*, 2002.
- [15] W. J. Staszewski, S. Mahzan, and R. Traynor, "Health monitoring of aerospace composite structures - Active and passive approach," *Composites Science and Technology*, vol. 69, pp. 1678-1685, 2009.
- [16] S. S. Kessler and S. M. Spearing, "Design of a piezoelectric-based structural health monitoring system for damage detection in composite materials," in *Smart Structures and Materials 2002: Smart Structures and Integrated Systems, 18-21 March 2002*, USA, 2002, pp. 86-96.
- [17] A. K. Mal, S. Banerjee, and F. Ricci, "Automated structural health monitoring system using acoustic emission and modal data," in *Health Monitoring and Smart Nondestructive Evaluation of Structural and Biological Systems III, March 15, 2004 - March 17, 2004*, San Diego, CA, United states, 2004, pp. 1-10.
- [18] M. A. Maseras-Gutierrez, W. J. Staszewski, M. S. Found, and K. Worden, "Detection of impacts in composite materials using piezoceramic sensors and neural networks," in *Smart Structures and Materials 1998: Smart Structures and Integrated Systems, February 3, 1998 - February 3, 1998*, San Diego, CA, United states, 1998, pp. 491-497.
- [19] D. W. Stinemas, C. R. Farrar, H. Sohn, and J. G. Bennett, "Structural health monitoring system design using finite element analysis," in *Smart Nondestructive Evaluation for Health Monitoring of Structural and Biological Systems, 18-20 March 2002*, USA, 2002, pp. 169-78.
- [20] H. Lamb, "On Waves in an Elastic Plate," *Proceedings of the Royal Society of London. Series A, Containing Papers of a Mathematical and Physical Character*, vol. 93, pp. 114-128, 1917.
- [21] D. C. Worlton, "Experimental confirmation of lamb waves at megacycle frequencies," *Journal of Applied Physics*, vol. 32, pp. 967-971, 1961.
- [22] D. N. Alleyne and P. Cawley, "The interaction of Lamb waves with defects," *Ultrasonics, Ferroelectrics and Frequency Control, IEEE Transactions on*, vol. 39, pp. 381-397, 1992.
- [23] R. Jha, I. Kim, and D. Widana-Gamage, "Investigation of Incident Lamb Wave Parameters on Detection of Composite Delamination," *ASME Conference Proceedings*, vol. 2010, pp. 675-683, 2010.
- [24] K. Diamanti, J. M. Hodgkinson, and C. Soutis, "Detection of Low-velocity Impact Damage in Composite Plates using Lamb Waves," *Structural Health Monitoring*, vol. 3, pp. 33-41, 2004.
- [25] A. Shelke, T. Kundu, U. Amjad, K. Hahn, and W. Grill, "Mode-selective excitation and detection of ultrasonic guided waves for delamination detection in laminated

- aluminum plates," *Ultrasonics, Ferroelectrics and Frequency Control, IEEE Transactions on*, vol. 58, pp. 567-577, 2011.
- [26] A. J. Croxford, P. D. Wilcox, B. W. Drinkwater, and G. Konstantinidis, "Strategies for guided-wave structural health monitoring," *Proceedings of the Royal Society A: Mathematical, Physical and Engineering Science*, vol. 463, pp. 2961-2981, 2007.
- [27] A. Raghavan and C. E. S. Cesnik, "Review of guided-wave structural health monitoring," *Shock and Vibration Digest*, vol. 39, pp. 91-114, 2007.
- [28] M. Majumder, T. K. Gangopadhyay, A. K. Chakraborty, K. Dasgupta, and D. K. Bhattacharya, "Fibre Bragg gratings in structural health monitoring—Present status and applications," *Sensors and Actuators A: Physical*, vol. 147, pp. 150-164, 2008.
- [29] R. J. Van Steenkiste and L. P. Kollar, "Effect of the coating on the stresses and strains in an embedded fiber optic sensor," *Journal of Composite Materials*, vol. 32, pp. 1680-1711, 1998.
- [30] Tikka Jarkko, Hedman Risto, and S. Aslak, "Strain gauge capabilities in crack detection," 4th International Workshop on Structural Health Monitoring, Stanford, CA, 2003.
- [31] S. Kessler, "Piezoelectric-based in-situ damage detection of composite materials for structural health monitoring systems," Massachusetts Institute of Technology Ph.D., Massachusetts Institute of Technology, United States -- Massachusetts, 2002.
- [32] K. Hegeon, G. M. Light, K. Sang-Young, and R. L. Spinks, "Magnetostrictive sensor for active health monitoring in structures," in *Smart Nondestructive Evaluation for Health Monitoring of Structural and Biological Systems, 18-20 March 2002, USA, 2002*, pp. 282-8.
- [33] S. Alag, A. M. Agogino, and M. Morjaria, "A methodology for intelligent sensor measurement, validation, fusion, and fault detection for equipment monitoring and diagnostics," (*AI EDAM*) *Artificial Intelligence for Engineering Design, Analysis and Manufacturing*, vol. 15, pp. 307-20, 2001.
- [34] M. I. Friswell and D. J. Inman, "Sensor Validation for Smart Structures," *Journal of Intelligent Material Systems and Structures*, vol. 10, pp. 973-982, 1999.
- [35] V. Giurgiutiu, "Lamb Wave Generation with Piezoelectric Wafer Active Sensors for Structural Health Monitoring," in *Smart Structures and Materials 2003: Smart Structures and Integrated Systems, March 3, 2003 - March 6, 2003*, San Diego, CA, United states, 2003, pp. 111-122.
- [36] IEEE, "IEEE Standard on Piezoelectricity 176," in *IEEE transactions on sonics and ultrasonics*, ed: IEEE, 1978.
- [37] S. S. Kessler, S. M. Spearing, and C. Soutis, "Damage detection in composite materials using Lamb wave methods," *Smart Materials and Structures*, vol. 11, pp. 269-278, 2002.

- [38] J. R. Wait, G. Park, H. Sohn, and C. R. Farrar, "Plate damage identification using wave propagation and impedance methods," in *Health Monitoring and Smart Nondestructive Evaluation of Structural and Biological Systems III, March 15, 2004 - March 17, 2004*, San Diego, CA, United states, 2004, pp. 53-65.
- [39] A. B. Thien, "Pipeline structural health monitoring using macro-fiber composite active sensors," University of Cincinnati, 2006.
- [40] S. Soni, S. Das, and A. Chattopadhyay, "Simulation of damage-features in a lug joint using guided waves," *Journal of Intelligent Material Systems and Structures*, vol. 20, pp. 1451-64, 2009.
- [41] G. Thursby, B. Culshaw, and D. C. Betz, "Multifunctional fibre optic sensors monitoring strain and ultrasound," *Fatigue & Fracture of Engineering Materials & Structures*, vol. 31, pp. 660-673, 2008.
- [42] K. Diamanti and C. Soutis, "Structural health monitoring techniques for aircraft composite structures," *Progress in Aerospace Sciences*, vol. 46, pp. 342-352, 2010.
- [43] M. C. Lafarie-Frenot and C. Hénaff-Gardin, "Formation and growth of 90° ply fatigue cracks in carbon/epoxy laminates," *Composites Science and Technology*, vol. 40, pp. 307-324, 1991.
- [44] N. Takeda and S. Ogihara, "Initiation and growth of delamination from the tips of transverse cracks in CFRP cross-ply laminates," *Composites Science and Technology*, vol. 52, pp. 309-318, 1994.
- [45] N. Toyama, J. Noda, and T. Okabe, "Quantitative damage detection in cross-ply laminates using Lamb wave method," *Composites Science and Technology*, vol. 63, pp. 1473-1479, 2003.
- [46] T. Yokozeki, T. Aoki, and T. Ishikawa, "Fatigue growth of matrix cracks in the transverse direction of CFRP laminates," *Composites Science and Technology*, vol. 62, pp. 1223-1229, 2002.
- [47] K. Amara, A. Tounsi, A. Megueni, and E. A. Adda-Bedia, "Effect of transverse cracks on the mechanical properties of angle-ply composites laminates," *Theoretical and Applied Fracture Mechanics*, vol. 45, pp. 72-78, 2006.
- [48] A. El-Kafrawy, "Crack detection by modal analysis in 3D beams based on FEM," *International Journal of Mechanics and Materials in Design*, vol. 7, pp. 265-282, 2011.
- [49] M. Chati, R. Rand, and S. Mukherjee, "Modal analysis of a cracked beam," *Journal of Sound and Vibration*, vol. 207, pp. 249-270, 1997.
- [50] S. Loutridis, E. Douka, and A. Trochidis, "Crack identification in double-cracked beams using wavelet analysis," *Journal of Sound and Vibration*, vol. 277, pp. 1025-1039, 2004.

- [51] I. Bartoli, "Structural health monitoring by ultrasonic guided waves," Ph.D. 3283893, University of California, San Diego, United States -- California, 2007.
- [52] S. S. Kessler, "Piezoelectric-based in-situ damage detection of composite materials for structural health monitoring systems," Ph.D. 0804717, Massachusetts Institute of Technology, United States -- Massachusetts, 2002.
- [53] H. M. Matt, "Structural diagnostics of CFRP composite aircraft components by ultrasonic guided waves and built-in piezoelectric transducers," Ph.D. 3238426, University of California, San Diego, United States -- California, 2006.
- [54] H. Gao and J. L. Rose, "Ultrasonic sensor placement optimization in structural health monitoring using evolutionary strategy " in *American Institute of Physics*, 2006.
- [55] W. Huyer and A. Neumaier, "SNOBFIT - Stable noisy optimization by branch and fit," *ACM Transactions on Mathematical Software*, vol. 35, 2008.
- [56] J. S. Hayward and B. Harris, "The effect of vacuum assistance in resin transfer moulding," *Composites Manufacturing*, vol. 1, pp. 161-166, 1990.
- [57] X. Song, "Vacuum assisted resin transfer molding (VARTM): Model development and verification," Ph.D. 3147766, Virginia Polytechnic Institute and State University, United States -- Virginia, 2003.
- [58] X. Sun, S. Li, and L. J. Lee, "Mold filling analysis in vacuum-assisted resin transfer molding. Part I: SCRIMP based on a high-permeable medium," *Polymer Composites*, vol. 19, pp. 807-817, 1998.
- [59] R. Chen, C. Dong, Z. Liang, C. Zhang, and B. Wang, "Flow modeling and simulation for vacuum assisted resin transfer molding process with the equivalent permeability method," *Polymer Composites*, vol. 25, pp. 146-164, 2004.
- [60] A. Utturkar, "Permeability modeling of symmetric graphite epoxy laminates with arbitrary ply orientations," M.S. 1427827, Oklahoma State University, United States - - Oklahoma, 2005.
- [61] E. Volterra and E. C. Zachmanoglou. (1965). *Dynamics of vibrations*.
- [62] A. S. Selvarathinam and Y. J. Weitsman, "A shear-lag analysis of transverse cracking and delamination in cross-ply carbon-fibre/epoxy composites under dry, saturated and immersed fatigue conditions," *Composites Science and Technology*, vol. 59, pp. 2115-2123, 1999.
- [63] J. R. Maddocks, "Microcracking in composite laminates under thermal and mechanical loading," M.S., Aeronautics and Astronautics, Massachusetts Institute of Technology, 1995.

- [64] Q.-M. Wang, X.-H. Du, B. Xu, and L. E. Cross, "Theoretical analysis of the sensor effect of cantilever piezoelectric benders," *Journal of Applied Physics*, vol. 85, pp. 1702-1712, 1999.
- [65] P. Ngerchuklin, B. Jadidian, E. K. Akdogan, and A. Safari, "PMN-PT piezoelectric-electrostrictive monolithic multi-material composite actuator," in *17th IEEE International Symposium on the Applications of Ferroelectrics, ISAF 2008, February 23, 2008 - February 28, 2008*, Santa Fe, NM, United states, 2008.
- [66] V. Giurgiutiu, "Tuned Lamb wave excitation and detection with piezoelectric wafer active sensors for structural health monitoring," *Journal of Intelligent Material Systems and Structures*, vol. 16, pp. 291-305, 2005.
- [67] R. F. Guratzsch, S. Mahadevan, C. L. Pettit, and M. M. Derriso, "Sensor placement optimization for shm systems under uncertainty," *46th AIAA/ASME/ASCE/AHS/ASC Structures, Structural Dynamics and Materials Conference, April 18, 2005 - April 21, 2005*, Austin, TX, United states, 2005, pp. 5182-5188.
- [68] "NASA technical report," The University of Alabama, 2012.

APPENDIX A: Conference contributions

A list of conference proceedings and presentations:

A. Nagabhushana, M. Spiegel, S. Adu, N. Hayes, D. Paul, K. Trivedi, B. Fairbee, H. Zheng, A. Gerrity, S. Kotru, S. Roy, M. Barkey, S.L. Burkett, *Numerical analysis for structural health monitoring of a damaged composite panel using PZT actuators and sensors*, Smart Structures and Materials – Non destructive evaluation and health monitoring, March 11-14, 2012, San Diego, CA, United States, SPIE.

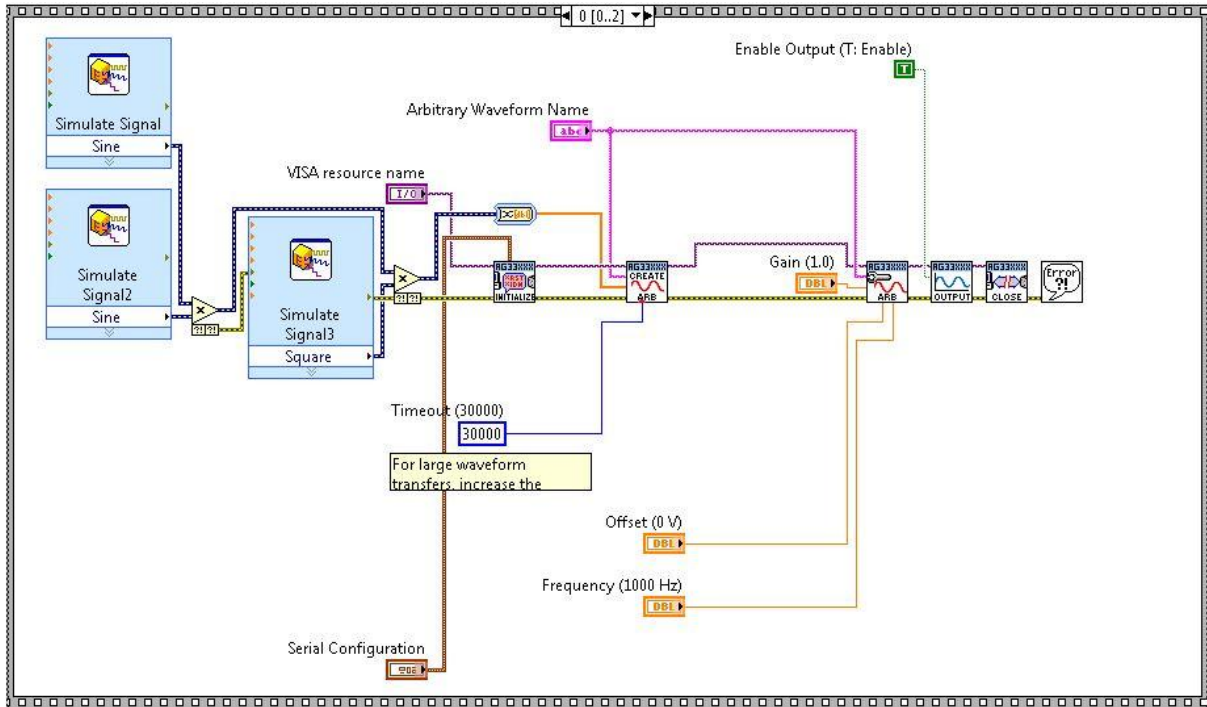
M. Farooq, H. Zheng, A. Nagabhushana, S. Roy, S.L. Burkett, E. Sazonov, *Damage detection and identification using support vector machines and neural networks*, Smart Structures and Materials – Non destructive evaluation and health monitoring, March 11-14, 2012, San Diego, CA, United States, SPIE.

M. Spiegel, A. Nagabhushana, S. Roy, S. L. Burkett and S. Kotru, *Structural Health Monitoring of Composite Materials using PZT Actuators and Sensors*, presented at the Research Seminar, Center for Materials for Information Technology, October, 2011, The University of Alabama, Tuscaloosa, Alabama, United States.

M. Rao, A. Nagabhushana, A. Sumant, R. Divan, J. C. Lusth, and S. L. Burkett, *Fabrication of carbon nanotube filled through silicon vias*, Global Interposer Technology Workshop, November 14-15, 2011, Atlanta, Georgia, United States.

APPENDIX B: LabVIEW program

LabVIEW program developed to write to arbitrary waveform generator to generate Hanning waveform input.



LabVIEW program developed to read from the DAQ.

